Weak-value-amplification enhancement of the magneto-optical Kerr effect in nanoscale layered structures

Jing-Hui Huang (黄鲸珲),[1,2,*] Jeff S. Lundeen,[2,†] Kyle M. Jordan,[2,‡] Adetunmise C. Dada,[3,§] Guang-Jun Wang (王广君),[4,‖] and Xiang-Yun Hu (胡祥云)[1,¶]

[1]*School of Geophysics and Geomatics, China University of Geosciences, Lumo Road 388, 430074 Wuhan, China*

[2]*Department of Physics and Centre for Research in Photonics, University of Ottawa, 25 Templeton Street, Ottawa, Ontario, Canada K1N 6N5*

[3]*School of Physics and Astronomy, University of Glasgow, Glasgow G12 8QQ, United Kingdom*

[4]*School of Automation, China University of Geosciences, Lumo Road 388, 430074 Wuhan, China*

(Received 26 June 2023; accepted 13 September 2023; published 29 September 2023)

The achievement of a larger magneto-optical Kerr effect (MOKE) in nanoscale layered structures is extremely important for both theoretical understandings and practical applications. However, nanoscale layered structures may not always exhibit enhanced MOKE under certain geometries. In this paper, we present a scheme based on weak-value amplification (WVA) for simultaneously detecting and enhancing the Kerr signals in nanoscale layered structures. The Kerr signals can be effectively amplified as the parameters of the preselection in WVA. We numerically investigate the dependence of the thickness d of Co in the sample HfO_2(10 nm)/Co(d nm)/HfO_2(30 nm)/Al(40 nm)/Si and the sample Co(d nm)/Si in the range of 5 nm $< d <$ 50 nm. Our results indicate that the combination of the cavity and WVA can simultaneously amplify the MOKE signals when compared to the application of WVA on the sample Co(d nm)/Si and the application of traditional MOKE setup (TMOKES) on the two samples. Importantly, our results highlight that WVA maintains its ability to amplify MOKE signals even in cases where the cavity in the TMOKES scheme fails to enhance the Kerr signals. This signifies the exceptional advantage of WVA in amplifying Kerr signals over TMOKES, regardless of the sample structures and specific MOKE geometries employed.

DOI: 10.1103/PhysRevA.108.033724

I. INTRODUCTION

The small rotation in a beam's polarization state by reflection from a magnetic surface, known as the magneto-optic Kerr effect (MOKE) [1], is widely used as a probe of magnetic materials. This effect originated in 1877, when Kerr examined the polarization of the light reflected from a polished electromagnet pole and found that the linear polarized light transforms into an elliptically polarized light as the consequence of MOKE [2]. In principle, MOKE is characterized by the complex magneto-optical (MO) Kerr angle $\phi_k = \theta_k + i\varepsilon$, where θ_k is the Kerr rotation, and ε is the Kerr ellipticity. Thus, the first application of MOKE was to study ultrathin Fe films grown epitaxially onto a single crystalline substrate of Au (100). Characteristic loops in MOKE due to hysteresis were measured with atomic layer sensitivity as a function of the Fe film thickness and temperature [3]. Furthermore, with the rapid advancement of modern surface science and nanoengineering [4–6], MOKE has been widely applied in studying the magnetization dynamics of magnetic materials [7,8], investigating the structure of the surface and interface [9–11], and even looking for the topological electromagnetic phase of matter [12,13].

Many approaches pursue higher precision for large Kerr angles in both theoretical understandings and practical applications. Melle *et al.* reported a strong increase of the MO properties of hexagonally arranged Ni nanowires with high absorption due to surface plasmon polariton excitation [14]. Jenkins *et al*. reported the first terahertz Kerr rotation on the topological insulator Bi_2Se_3 at extreme experimental conditions ($T = 10$ K, $B = 8$ T) [15]. The multilayer structures [16] like HfO_2/Co/HfO_2/Al/Si [17], SnO_2/Co/SnO_2/Al/Si [18], and glass/Al/SnO_2/PtMnSb/SnO_2 [19] have shown the advantages for increasing the Kerr angle. Furthermore, the recent development of MO all-dielectric resonators and metasurfaces show promising potential for enhancing the MOKE in continuous films by observing surface plasmon resonance modes [20–22]. Their performance is highly dependent on the unique structures and the specific wavelength range. Therefore, it is challenging to ensure that the chosen measurement conditions or schemes will consistently achieve MOKE enhancement across diverse nanoscale structures. While the enhancement of MOKE in traditional cavities and magnetoplasmonics is an exciting field of study, this paper primarily focuses on advancing the sensitivity of measurements for a broader range of nanoscale layered structures.

*jinghuihuang@cug.edu.cn
†jeff.lundeen@gmail.com
‡kjordan@uottawa.ca
§Adetunmise.Dada@glasgow.ac.uk
‖gjwang@cug.edu.cn
¶xyhu@cug.edu.cn

Weak-value amplification (WVA) has established itself as a powerful and widely adopted technique in the field of precision metrology [23–30]. WVA with postselection was initially introduced by Aharonov *et al*., demonstrating its ability to amplify the measurement outcome of a spin-1/2 particle by a factor of 100 [31]. Subsequently, numerous studies confirmed the effectiveness of WVA in amplifying small parameters for the detection of various physical properties [32–37]. Therefore, WVA as a novel signal-enhanced technique can potentially strengthen the MOKE [38–42]. Li *et al*. studied an enhanced spin Hall effect (SHE) of light in MO oxide thin films under the transverse MOKE configuration [39]. Wang *et al*. obtained the precision of about 10^{-6} rad for hysteresis loop measurement under ordinary experimental conditions by using the SHE and WVA [40]. He *et al*. proposed a nonlinear weak measurement scheme for MO Kerr signals in single-layer MO structure with a frequency pointer [41]. Luo *et al*. demonstrated the Kerr angle can be directly obtained using the product of the light intensity and the amplified displacement shift in a weak measurement method using two pointers [42]. While the application of WVA to MOKE measurements has been explored extensively for simple sample configurations in previous studies [38–42], research is increasingly focused on complex magnetic heterostructures, which may contain cavity structures to enhance the optical response. A complete understanding of the practical use of WVA for MOKE measurements must therefore consider more complicated structures in addition to the simple monolayers of previous research. In this case, it is possible to obtain an enhanced sensitivity due to either WVA or the resonant response, or a combination of both, depending on the particular parameters of the sample and the probe beam.

In this paper, we theoretically investigate both the MO polar Kerr properties and the MO longitudinal Kerr properties in nanoscale layered structures based on WVA. The interaction described by the boundary and transmission matrix [43] between the light and the magnetic films can be regarded as parameters of the preselected state [40,41,44], then Kerr rotation θ_k and Kerr ellipticity ε can be simultaneously amplified by choosing the appropriate postselected state and the coupling strength in WVA. Furthermore, we show the amplification of the Kerr signals in WVA when compared with both the traditional MOKE setup and the cavity technique [1]. Specifically, we model the dependence on thickness d of Co in sample HfO_2(10 nm)/Co(d nm)/HfO_2(30 nm)/Al(40 nm)/Si and sample Co(d nm)/Si in the range of 5 nm $< d <$ 50 nm. The results of the dependence of thickness d of Co in various structures indicate that the postselected state needs to be carefully prepared to avoid the nonmonotonicity between the measurement result and the thickness of Co film. The final simulation results confirm that the combination of the cavity and WVA can further amplify the MOKE signals, and the enhancement in various cases is more prominent with higher sensitivities at a measurement range of 5 nm $< d <$ 15 nm. It is worth noting that WVA shows the ability to enhance the MOKE signals, even when the cavity fails to amplify the Kerr signals.

The paper is organized as follows. In Sec. II, we introduce the standard WVA with the longitudinal pointers for MOKE detection in nanoscale layered structures. In Sec. III, we briefly review the application of WVA to the Kerr signals and compare the WVA setup to the traditional MOKE measurement scheme. In Sec. IV A, we give the results of numerical modeling of WVA with the various postselections when applied to the layered structure HfO_2/Co/HfO_2/Al/Si. In Sec. IV B, we investigate the dependence on thickness d of Co with the sample HfO_2(10 nm)/Co(d nm)/HfO_2(30 nm)/Al(40 nm)/Si. In Sec. IV C 3, the advantage of the WVA technique is studied. Section V consists of a summary.

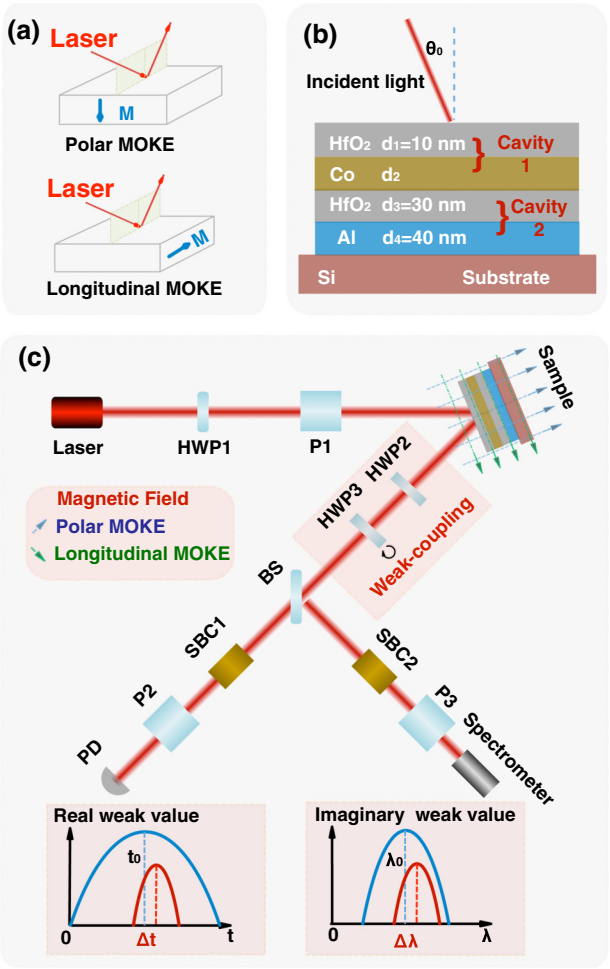

FIG. 1. (a) The directions of the magnetic field (M) in the polar geometry and the longitudinal geometry for the MOKE detection. (b) Schematic of the nanoscale layered structure HfO_2(10 nm)/Co(d nm)/HfO_2(30 nm)/Al(40 nm)/Si films. (c) Scheme of WVA for MOKE detection. Laser, Gaussian-shaped laser with central wavelength $\lambda_0 = 632.8$ nm; HWP, half-wave plate; $P1$, $P2$, and $P3$, polarizers; BS, beam splitter (ratio 50 : 50); SBC1 and SBC2, Soleil-Babinet compensators; PD, Photo diode.

II. WVA FOR THE MOKE DETECTION

For the numerical modeling of the MOKE enhancement in nanoscale layered structures, the multilayer of HfO_2/Co/HfO_2/Al films on Si substrates is studied and the structure is shown in Fig. 1(b). There are two Fabry-Perot cavities [45] to enhance the Kerr effect in this structure. The

first cavity is composed of HfO_2 and the optically anisotropic Co layer and the other one consists of two metallic layers Co and Al which act as two mirrors with the interlayer HfO_2 acting as a dielectric medium. In addition, the directions of the magnetic field (M) in the polar MOKE and the longitudinal MOKE geometries are displayed in Fig. 1(a). The transverse geometry for the MOKE has been seldom investigated because the polarization of the reflected light does not change and only the relative change in intensity can be measured in the transverse MOKE [46,47]. Note that the work [1] indicated that the larger the incident angle θ_0 is in the polar geometry and the smaller θ_0 is in the longitudinal geometry, the weaker the MOKE. To highlight the advantages of WVA, the MOKE system is working in the polar geometry with $\theta_0 = 80^\circ$ and the longitudinal geometry with $\theta_0 = 3^\circ$. The specific scheme of WVA for the MOKE detection is shown in Fig. 1(c), WVA includes the initial preparation of the measured system (pre-selection), a weak coupling between the system and the pointer (weak-coupling), a postselection on the system (postselection) and a projective measurement on the pointer to read out the measurement results (readout of weak value). In sequence, the following sections of our article will cover the four steps in detail.

A. Preselection

The preselection is achieved by the beam with central wavelength λ_0 passing through an HWP, a polarizer ($P1$) and the interaction between the light and the MO sample, where the HWP is used to adjust the intensity of the incident light, and $P1$ is designed to prepare the system at the horizontally polarized state

$$|\Psi_i\rangle = \sin(\alpha)|H\rangle + \cos(\alpha)|V\rangle, \tag{1}$$

with $\alpha = \pi/2$. Here, $|H\rangle$ and $|V\rangle$ represent the horizontally and vertically polarized states, respectively. Note that the states $|H\rangle$ and $|V\rangle$ are obtained in the basis

$$\begin{aligned} |H\rangle &= (|\nearrow\rangle + |\searrow\rangle)/\sqrt{2}, \\ |V\rangle &= (|\nearrow\rangle - |\searrow\rangle)/\sqrt{2}. \end{aligned} \tag{2}$$

Figure 2 shows the location in the Poincaré sphere, where the states $|\nearrow\rangle$ and $|\searrow\rangle$ are orthogonal. The state $|\nearrow\rangle(|\searrow\rangle)$ represents the linearly polarized light beam, which is at an angle of $+\pi/2(-\pi/2)$ to the horizontal state $|H\rangle$ in the Poincaré sphere representations in Fig. 2.

When the light is reflected from the MO sample, the state $|\Psi_i\rangle$ will change slightly to the state $|\Psi_w\rangle$ (shown in Fig. 2) on the Poincaré sphere due to the MOKE. In the MOKE study for layered structures, the universal approach to calculate MO coefficients in a multilayered system is based on the boundary matrix **A** and the transmission matrix **D** [1,43,48]. The boundary matrix **A** is a 4×4 matrix, which relates the tangential components of the electric and magnetic with the s and p components of the electric field. The transmission 4×4 matrix **D** relates the s and p components of the electric field at two surfaces of a film of thickness d [1]. The boundary matrix **A** and the transmission matrix **D** for both the longitudinal (L) case and polar (P) case are displayed in Appendix A. In this paper, each layer is characterized by its refractive index

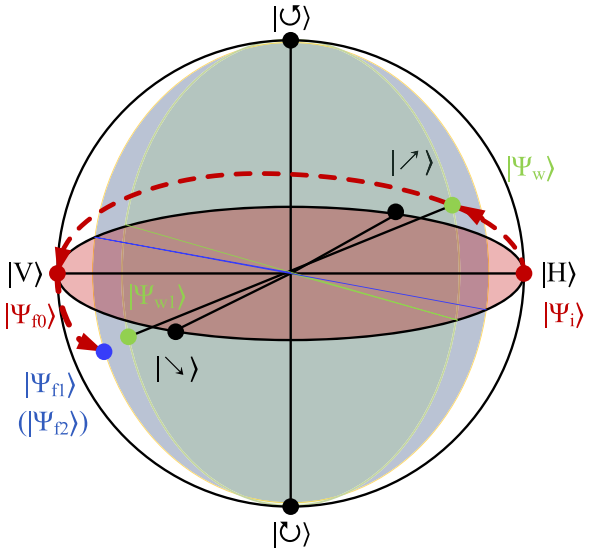

FIG. 2. The Poincaré sphere showing the preselected state $|\Psi_w\rangle$ and postselected states $|\Psi_{f0}\rangle$, $|\Psi_{f1}\rangle$, and $|\Psi_{f2}\rangle$ with various strategies.

($N_i = n + ik$), MO coupling constant ($Q_i = Q_r + iQ_i$) and the layer thickness d_i. Thus, the total reflective matrix for the nanoscale layered structure can be calculated as follows:

$$\mathbf{M} = \mathbf{A}_{\text{Air}}^{-1} \prod_i \mathbf{A}_i \mathbf{D}_i \mathbf{A}_i^{-1} \mathbf{A}_f = \begin{pmatrix} \mathbf{G} & \mathbf{H} \\ \mathbf{I} & \mathbf{J} \end{pmatrix}. \tag{3}$$

Here, $\mathbf{A}_{\text{Air}}$ and $\mathbf{A}_f$ are the boundary matrices for the interface of air and the final layer. The comprehensive definitions of matrices **A** and **D** can be found in Appendix A. The matrices **G** and **I** are 2×2 block matrices and correspond to a portion of the final calculation result of Eq. (3). In the MOKE study, because of the optical anisotropy, the Fresnel coefficients (including r_{pp}, r_{ps}, r_{sp}, and r_{ss}) can be calculated from

$$\mathbf{IG}^{-1} = \begin{pmatrix} r_{pp} & r_{ps} \\ r_{sp} & r_{ss} \end{pmatrix}. \tag{4}$$

Thus, the polarization state after the light passes through the MO sample is defined as

$$\begin{aligned} |\Psi_w\rangle &= r_{pp}|H\rangle + r_{sp}|V\rangle \\ &\approx \frac{1}{\sqrt{2}} r_{pp}(e^{\theta_k + i\varepsilon}|\nearrow\rangle + e^{-\theta_k - i\varepsilon}|\searrow\rangle). \end{aligned} \tag{5}$$

Then the Kerr rotation θ_k and the Kerr ellipticity ε can be calculated from the Fresnel coefficients $r_{sp}/r_{pp} = \theta_k + i\varepsilon$. Note that the approximation in Eq. (5) is obtained with the limit $r_{sp}/r_{pp} = \theta_k + i\varepsilon \ll 1$, the weak-coupling limit in which WVA works. Meanwhile, the pointer's wave function is prepared and simultaneously shaped in the time and frequency domains by the laser system. The laser in the time domain has the Gaussian profile

$$|\langle t|\Phi_i\rangle|^2 = \left(\frac{1}{2\pi(\Delta t)^2}\right)^{\frac{1}{2}} e^{-\frac{(t-t_0)^2}{2(\Delta t)^2}}. \tag{6}$$

At the same time, the pointer in the frequency domain is simultaneously determined according to the Fourier transform

$$|\langle\omega|\Phi_i\rangle|^2 = \left|\int dt\,|\langle t|\Phi_i\rangle|e^{i\omega t}\right|^2 = \pi(\Delta t)^2\left(\frac{1}{2\pi(\Delta t)^2}\right)^{\frac{1}{2}} e^{-2(\Delta t)^2(\omega-\omega_0)^2} = \left(\frac{\pi}{8(\Delta\omega)^2}\right)^{\frac{1}{2}} e^{-\frac{(\omega-\omega_0)^2}{2(\Delta\omega)^2}}, \tag{7}$$

where Δt and $\Delta\omega$ represent the width of the Gaussian wave packet in the time and frequency domains, respectively. Note that Eq. (7) indicates that the time-bandwidth product $\Delta t \times \Delta\omega$ must satisfy the transform-limited relationship $\Delta t \times \Delta\omega = 1/2$ for a Gaussian-shaped laser [49–52]. Meanwhile, considering the relationship $\omega = c/\lambda$ between the frequency and the wavelength of light, the variances of the temporal pulse and its spectrum will always interact by

$$\Delta t\,\Delta\omega = \Delta t\left(c\Delta\lambda/\lambda_0^2\right) = 1/2. \tag{8}$$

Therefore, the widths of the laser in the time and the frequency domains need to be carefully chosen for measuring the two pointer shifts.

B. Weak coupling

The combination of two half-wave plates [HWP2 and HWP3 in Fig. 1(c)] has been successfully applied as the "weak coupling" in standard weak measurement [53–55]. Conceptually, the weak interaction is achieved by placing two identical true zero-order HWPs, one perpendicular and one almost perpendicular but with a tiny tilt β_w [53]. Therefore, the weak interaction between the polarization and the temporal degrees of freedom of photons is described by a unitary operator $\hat{U} = \exp(-ig\hat{p}\otimes\hat{A})$, where the momentum operator $\hat{p}$ is the frequency in the spectrum of the pointer light. The weak-coupling strength $g = \chi_w/p_0$ is related to the phase shift χ_w and p_0 is the photon momentum $p_0 = 2\pi/\lambda_0$. In addition, the phase shift χ_w and the tiny tilt β_w has the following relationship, as given by Ref. [53]

$$\chi_w = \pi\left(\frac{1}{(1-\sin^2\beta_w/n_0^2)^{1/2}} - 1\right) \approx \frac{\pi\beta_w^2}{2n_0^2}, \tag{9}$$

where $n_0 = 1.54$ is the refractive index of the HWPs. The small phase $\chi_w \ll 1$ rad is required to keep the measurement working on the "weak-coupling" domain.

C. Postselection

In principle, by preparing the appropriate final state $|\Psi_f\rangle$, the degree of the amplification is quantified by the so-called weak value, which is defined as $A_w := \langle\Psi_f|\hat{A}|\Psi_w\rangle/\langle\Psi_f|\Psi_w\rangle$ with $\hat{A} = |\nearrow\rangle\langle\nearrow| - |\searrow\rangle\langle\searrow|$. When the states $|\Psi_w\rangle$ and $|\Psi_f\rangle$ are nearly orthogonal, the weak value can significantly exceed the normal eigenvalue and lead to an amplified pointer shift, at a cost that the probability $\Pi_w = |\langle\Psi_f|\Psi_w\rangle|^2$ of successful postselection decreases. In this paper, the small Kerr rotation θ_k and the Kerr ellipticity ε regarded as parameters of $|\Psi_w\rangle$ are related to the weak value and amplified by choosing the appropriate postselection state $|\Psi_f\rangle$. It can be found that numerous studies [40,41,44] also chose the amplification of parameters regarded as the preselected angle in WVA, which is only related to the imaginary part of the weak value in the frequency domain. Note that this scenario differs from the traditional parameters amplification of the coupling strength in WVA [31,32,35,55]. The amplification by the factor A_w of Kerr signals θ_k and ε with various postselections is discussed in the following. Furthermore, Sec. III shows the amplification of the Kerr signals in WVA when compared to the traditional MOKE setup.

Normally, the postselection state $|\Psi_f\rangle$ is given by $|\Psi_{f0}\rangle = |V\rangle = (|\nearrow\rangle - |\searrow\rangle)/\sqrt{2}$, where $|\Psi_{f0}\rangle$ is orthogonal to the preselection state $|\Psi_i\rangle$ and the states $|\Psi_w\rangle$ and $|\Psi_{f0}\rangle$ are nearly orthogonal. This paper calls this strategy "fully orthogonal" (FO) postselection. However, we reselect $|\Psi_f\rangle$ and mark the different strategy as non-FO postselection, where $|\Psi_f\rangle$ slightly deviates from $|\Psi_{f0}\rangle$ as shown in Fig. 2. The preselection state $|\Psi_w\rangle$ and postselection state $|\Psi_{f0}\rangle$ lead to a weak value

$$A_{w0} = \frac{\langle\Psi_{f0}|\hat{A}|\Psi_w\rangle}{\langle\Psi_{f0}|\Psi_w\rangle} = \frac{e^{+\theta_k+i\varepsilon} + e^{-\theta_k-i\varepsilon}}{e^{+\theta_k+i\varepsilon} - e^{-\theta_k-i\varepsilon}} = \mathrm{Re}A_{w0} + i\mathrm{Im}A_{w0}, \tag{10}$$

where $\mathrm{Re}A_{w0}$ and $\mathrm{Im}A_{w0}$ represent the real part and the imaginary part of the weak value, respectively. It is not convenient to directly measure the imaginary part of the physical quantities (e.g., the Kerr ellipticity ε and the imaginary part of A_{w0}) with the traditional methods [1]. In the previous work [1,41], another measurement, conducted by placing a quarter-wave plate before the analyzing polarizer, is needed to interchange the Kerr rotation and the Kerr ellipticity, i.e., the quarter-wave plate will produce a $\pi/2$ phase difference between the s and p components so that the analyzing polarizer will see $i(-\theta_k - i\varepsilon) = -\varepsilon - i\theta_k$. In addition, we show the traditional MOKE setup (TMOKES) for detecting the Kerr ellipticity ε in Sec. III. Another way to measure the imaginary part is to conduct the WVA in the momentum domain (here, a role played by frequency) [23]. Building on this, we introduce and study simultaneous time and frequency measurements to find the real and imaginary parts, the Kerr rotation and ellipticity.

Equation (10) indicates that θ_k and ε can be evaluated from the real part $\mathrm{Re}A_{w0}$ and the imaginary part $\mathrm{Im}A_{w0}$:

$$\theta_k = \frac{1}{\mathrm{Re}A_{w0} - 2 + \frac{\mathrm{Im}A_{w0}^2}{\mathrm{Re}A_{w0}} + \frac{1}{\mathrm{Re}A_{w0}}} \xrightarrow[\mathrm{Re}A_{w0}\gg 1]{\mathrm{Re}A_{w0}/\mathrm{Im}A_{w0}\gg 1} \theta_k \approx \frac{1}{\mathrm{Re}A_{w0}}, \tag{11}$$

$$\varepsilon = -\frac{1}{2}\mathrm{ArcTan}\left(\frac{2}{-\frac{1}{\mathrm{Im}A_{w0}} + \frac{\mathrm{Re}A_{w0}^2}{\mathrm{Im}A_{w0}} + \mathrm{Im}A_{w0}}\right) \xrightarrow[\mathrm{Im}A_{w0}\gg 1]{\mathrm{Re}A_{w0}/\mathrm{Im}A_{w0}\ll 1} \varepsilon \approx -\frac{1}{\mathrm{Im}A_{w0}}. \tag{12}$$

Equations (11) and (12) show the principle of the amplification of the Kerr rotation θ_k and ellipticity ε. For this FO postselection, θ_k is amplified and equals to $1/\mathrm{Re}A_{w0}$ with the conditions $\mathrm{Re}A_{w0}/\mathrm{Im}A_{w0} \gg 1$ and $\mathrm{Re}A_{w0} \gg 1$, namely,

the tiny θ_k will lead to a large $\mathrm{Re}A_{w0}$. Similarly, ε can be amplified and equals to $-1/\mathrm{Im}A_{w0}$ with the conditions $\mathrm{Re}A_{w0}/\mathrm{Im}A_{w0} \ll 1$ and $\mathrm{Im}A_{w0} \gg 1$. Apparently, the simultaneous achievement of the two conditions $\mathrm{Re}A_{w0}/\mathrm{Im}A_{w0} \gg 1$ and $\mathrm{Re}A_{w0}/\mathrm{Im}A_{w0} \ll 1$ is a contradiction in this FO postselection. Therefore, to simultaneously measure θ_k and ε with the two different approximation conditions, the postselection state needs to be reselected with a different strategy.

Then, we further study the optimal state $|\Psi_f\rangle$ with the strategy of non-FO postselection. There are three reasons why we need to optimize $|\Psi_f\rangle$ beyond the FO postselection described above. First, Eq. (10) indicates that A_w is inversely proportional to the probability Π_w. Therefore, WVA cannot be arbitrarily large in practice, $|\Psi_f\rangle$ needs to be carefully prepared for satisfying the detection limit. Second, within the dynamic range of the measurement, there should be a monotonic relationship between the measured quantity and the result. Third, two different postselection strategies need to be conducted for satisfying the approximation conditions $\mathrm{Re}A_{w0}/\mathrm{Im}A_{w0} \gg 1$ and $\mathrm{Re}A_{w0}/\mathrm{Im}A_{w0} \ll 1$, respectively. Therefore, we use different postselection schemes to get the nearly pure real A_w in the time domain and the nearly pure imaginary A_w in the frequency domain as shown in Fig. 1(c). Specifically, the light path with SBC1 and P2 postselects the system at state $|\Psi_{f1}\rangle$, and the path with SBC2 and P3 postselects the system at state $|\Psi_{f2}\rangle$:

$$|\Psi_{f1,f2}\rangle = \frac{1}{\sqrt{2}}\cos\left(\frac{\pi}{4}+\gamma_{1,2}\right)e^{i\eta_{1,2}}|\nearrow\rangle - \frac{1}{\sqrt{2}}\sin\left(\frac{\pi}{4}+\gamma_{1,2}\right)e^{-i\eta_{1,2}}|\searrow\rangle, \tag{13}$$

where the phase difference η_1 (η_2) between $|\nearrow\rangle$ and $|\searrow\rangle$ is induced by the SBC1 (SBC2), and γ_1 (γ_2) represents the angle between the polarization direction of P2 (P3) and the orthogonal polarization direction of P1. The final polarization $|\Psi_{f1,f2}\rangle$ leads to two different weak values

$$A_{w1,w2} = \frac{\langle\Psi_{f1,f2}|\hat{A}|\Psi_w\rangle}{\langle\Psi_{f1,f2}|\Psi_w\rangle} = \frac{\cos(\Gamma_{1,2})e^{-i\eta_{1,2}+\phi_k} + \sin(\Gamma_{1,2})e^{i\eta_{1,2}-\phi_k}}{\cos(\Gamma_{1,2})e^{-i\eta_{1,2}+\phi_k} - \sin(\Gamma_{1,2})e^{i\eta_{1,2}-\phi_k}}, \tag{14}$$

where $\phi_k = \theta_k + i\varepsilon$ is the complex MO Kerr angle and $\Gamma_{1,2} = \frac{\pi}{4} + \gamma_{1,2}$. Note that the relationship of the amplification of θ_k and ε based on weak value is more complicated than Eqs. (11) and (12) with the FO postselection. The approximate solutions of θ_k and ε are derived in Appendix C. So we obtain the approximate solutions with different approximation conditions

$$\theta_k \approx \frac{1}{4}\frac{2[1+\cos^2(2\gamma_1)]}{\mathrm{Re}A_{w1} - 2 + \frac{\mathrm{Im}A_{w1}{}^2}{\mathrm{Re}A_{w1}} + \frac{1}{\mathrm{Re}A_{w1}}} \xrightarrow[\mathrm{Re}A_{w1}\gg 1]{\frac{\mathrm{Re}A_{w1}}{\mathrm{Im}A_{w1}}\gg 1} \theta_k \approx \frac{1+\cos^2(2\gamma_1)}{2\mathrm{Re}A_{w1}}, \tag{15}$$

$$\varepsilon \approx \eta_2 - \frac{[1+\cos^2(2\gamma_2)]/2}{-\frac{2\cos^2(2\gamma_2)}{\mathrm{Im}A_{w2}}\left(\mathrm{Re}A_{w2}{}^2+1\right) + \mathrm{Im}A_{w2} + \mathrm{Re}A_{w2}} \xrightarrow[\mathrm{Im}A_{w2}\gg 1]{\frac{\mathrm{Re}A_{w2}}{\mathrm{Im}A_{w2}}\ll 1} \varepsilon \approx \eta_2 - \frac{1+\cos^2(2\gamma_2)}{2\mathrm{Im}A_{w2}}. \tag{16}$$

The first approximations in Eqs. (15) and (16) are achieved with the condition $\cos(4\gamma) = 1$ when $\gamma \to 0$. The second approximation in Eq. (15) is obtained by assuming $\mathrm{Re}A_{w1}/\mathrm{Im}A_{w1} \gg 1$ and $\mathrm{Re}A_{w1} \gg 1$, while the second approximation in Eq. (16) requires $\mathrm{Re}A_{w1}/\mathrm{Im}A_{w1} \ll 1$ and $\mathrm{Im}A_{w1} \gg 1$. Therefore, we can conclude that, for simultaneously detecting the Kerr signals, the weak value A_{w1} will be expected as a nearly pure real number with $\mathrm{Re}A_{w1}/\mathrm{Im}A_{w1} \gg 1$ for the amplification of θ_k, while the amplification of ε can be conducted by finding a nearly pure imaginary A_{w2} with $\mathrm{Re}A_{w1}/\mathrm{Im}A_{w1} \ll 1$.

D. Readout of weak value

In WVA, the real part of A_w characterizes the pointer's time shift δt and the imaginary part of A_w characterizes the pointer's frequency shift δp. Following the study in Ref. [56], the expectation value of the pointer shifts both in the two domains can be calculated from

$$\delta t = \frac{\frac{g}{c}\mathrm{Re}\,A_w}{1+\frac{1}{2}(e^{-2g^2\Delta p^2}-1)(1-|A_w|^2)} \approx \frac{g}{c}\mathrm{Re}\,A_w \ (g\Delta p \ll 1), \tag{17}$$

$$\delta p = \frac{2(\Delta p)^2 g\,\mathrm{Im}\,A_w e^{-2g^2\Delta p^2}}{1+\frac{1}{2}(e^{-2g^2\Delta p^2}-1)(1-|A_w|^2)} \approx 2(\Delta p)^2 g\,\mathrm{Im}\,A_w \ (g\Delta p \ll 1). \tag{18}$$

Note that the clearer and concise forms of δt and δp are obtained with $g\Delta p \ll 1$. In addition, the tiny tilt β_w [defined in Eq. (9)] satisfies the above condition and makes WVA working in the linear-like region [57]. Using the relationship between the momentum and the wavelength $\lambda = 2\pi/p$, $\delta p = -(2\pi/\lambda^2)\delta\lambda$, the shift of the central wavelength can be calculated by

$$\delta\lambda = -4\pi g\,\mathrm{Im}\,A_w(\Delta\lambda)^2/\left(\lambda_0^2\right). \tag{19}$$

According to the calculation of δt (17) and $\delta\lambda$ (19), $\mathrm{Re}A_w$ can be obtained on the PD by measuring the temporal shift, while $\mathrm{Im}A_w$ can be obtained on the spectrometer by measuring the wavelength shift.

III. COMPARISON OF WVA AND THE TRADITIONAL MOKE SETUP

There are several ways to build a MOKE setup for obtaining Kerr signals [1,4–6]. The simplest scheme, is found in Ref. [1] and shown in Fig. 3. In this section, we review the basic operation of the WVA measurement, which is then examined in more detail in Sec. IV.

The previous studies [39–41] showed that the WVA technique could strengthen the MOKE by detecting the transverse displacements of the WVA pointers. In this paper, we further numerically investigate the amplification of the MOKE in WVA when compared to the traditional MOKE setup (TMOKES) [1]. Figures 3(a) and 3(b) show the schematic with TMOKES of the Kerr rotation θ_k measurement and the Kerr ellipticity ε measurement, respectively. Note that the schematic in Fig. 3(a) is part of the WVA scheme in Fig. 1(c) without the "weak coupling" and "postselection." Therefore,

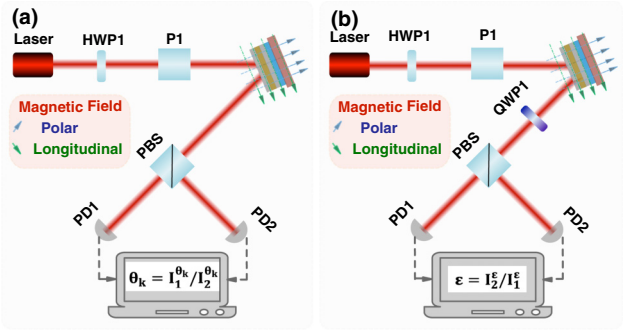

FIG. 3. Schematic of MOKE detection with the traditional simple MOKE setup. (a) The measurement of the Kerr rotation θ_k; (b) the measurement of the Kerr ellipticity ε; QWP1, a quarter-wave plate. Other components are the same as those used in Fig. 1(c).

the state of light after passing the MO sample is also prepared at $|\Psi_w\rangle$ in Eq. (5). Then the two components $|\nearrow\rangle$ and $|\searrow\rangle$ are separated by the polarizing beam splitter (PBS). Finally, the Kerr rotation θ_k can be estimated by calculating the ratio of the intensity $I_1^{\theta_k}$ detected on PD1 to the intensity $I_2^{\theta_k}$ detected on PD2

$$\frac{I_1^{\theta_k}}{I_2^{\theta_k}} = \frac{|e^{\theta_k + i\varepsilon}|^2}{|e^{-\theta_k - i\varepsilon}|^2} = e^{4\theta_k}. \tag{20}$$

Similarly, the Kerr ellipticity ε can be measured by inserting a quarter-wave plate (QWP) between the MO sample and PBS as shown in Fig. 3(b). Where QWP will produce a $\pi/2$ phase difference between $|\nearrow\rangle$ and $|\searrow\rangle$ components. Then, the Kerr ellipticity ε can be estimated by calculating the ratio of I_2^{ε} to I_1^{ε}:

$$\frac{I_2^{\varepsilon}}{I_1^{\varepsilon}} = \frac{|e^{-i\theta_k + \varepsilon}|^2}{|e^{+i\theta_k - \varepsilon}|^2} = e^{4\varepsilon}. \tag{21}$$

Equations (20) and (21) show the simplest way to measure the Kerr signals with TMOKES, where θ_k and ε are measured by the qualities $I_1^{\theta_k}/I_2^{\theta_k}$ and $I_2^{\varepsilon}/I_1^{\varepsilon}$, respectively. When comparing the measurement of WVA in Sec. II, θ_k and ε are related to the real and imaginary parts of weak value with an arbitrary postselection

$$\begin{aligned}
\mathrm{Re}A_w &= \frac{[\cos(\gamma) - \sin(\gamma)]^2 e^{2\theta_k} - [\cos(\gamma) + \sin(\gamma)]^2 e^{-2\theta_k}}{[\cos(\gamma) - \sin(\gamma)]^2 e^{2\theta_k} + [\cos(\gamma) + \sin(\gamma)]^2 e^{-2\theta_k} + 2\cos(2\gamma)\cos(\varepsilon - \eta)}, \\
\mathrm{Im}A_w &= \frac{-2\cos(2\gamma)\sin[2(\varepsilon - \eta)]}{[\cos(\gamma) - \sin(\gamma)]^2 e^{2\theta_k} + [\cos(\gamma) + \sin(\gamma)]^2 e^{-2\theta_k} + 2\cos(2\gamma)\cos(\varepsilon - \eta)}.
\end{aligned} \tag{22}$$

Furthermore, Fig. 4 display the amplification of the Kerr signals in WVA with the idea approximations of Eqs. (11) and (12). It can be found in Fig. 4(a) that the real part $\mathrm{Re}A_w$ is larger than the ratio $I_1^{\theta_k}/I_2^{\theta_k}$ in TMOKES when $\theta_k < 0.3$ rad, and WVA can estimate the greater magnification when θ_k gets smaller. In addition, the same results can be obtained from Fig. 4(b) for measuring the Kerr ellipticity ε. Note that the results of WVA in Fig. 4 are calculated with the idea approximations of Eqs. (11) and (12). The real part $\mathrm{Re}A_w$ and imaginary part $\mathrm{Im}A_w$ are related to the parameters γ and η and should be evaluated by Eqs. (22), respectively. Therefore, the amplification of the Kerr signals in WVA with non-FO postselection will be smaller than the ideal case, and the results with the most appropriate postselection are discussed in Sec. IV C 3.

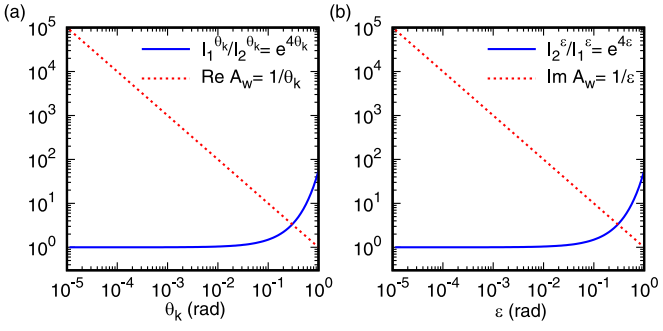

FIG. 4. The amplification of Kerr signals in WVA when compared with TMOKES. (a) The measurement of the Kerr rotation θ_k; (b) the measurement of the Kerr ellipticity ε.

IV. SIMULATION AND DISCUSSION

To demonstrate the advantage of WVA for enhancing the MOKE in nanoscale layered structures, the simulation of WVA for measuring the MOKE signals in the polar geometry with $\theta_0 = 80^\circ$ and in the longitudinal geometry with $\theta_0 = 3^\circ$ for measuring the sample $HfO_2(10\,\mathrm{nm})/Co(d\,\mathrm{nm})/HfO_2(30\,\mathrm{nm})/Al(40\,\mathrm{nm})/Si$ films and the sample $Co(d\,\mathrm{nm})/Si$ films were investigated. Thereinto, all the optical constants were taken from the refractive index database [58]. The MO coupling constants were taken from the literature [59]. The central wavelength of the incidence light was chosen at $\lambda_0 = 632.8$ nm. To simulate more realistic experimental conditions and find the appropriate postselected state, we considered the limitations of the performance of P2, P3, SBC1, SBC2, PD, and spectrometer. First, the minimum step size of the polarizers (P2 and P3) cannot be infinitely small [60]. In this paper, the minimum step size of the polarizers is assumed as 0.002 rad, and the rotation of $\gamma = -0.002$ rad, 0.000 rad, and 0.002 rad on the final state was investigated. Second, the Soleil-Babinet compensators (SBC1 and SBC2) are responsible for inducing continuously variable retardance from 0 to 2π rad [61]. Third, the detection limit of detectors is due to the dark current and spectrum. Thus, we assumed that WVA failed to detect the final signal when the probability $\Pi_w < 1.0 \times 10^{-5}$. To obtain the time shift δt Eq. (17) and

the wavelength shift $\delta\lambda$ Eq. (19), the weak coupling strength was set at $g = 6.6706 \times 10^{-9}$ when choosing $\beta_w = 0.3$ rad. The widths of the laser system were chosen at $\Delta\lambda = 20$ nm and $\Delta t = 33$ fs. In this setup, time shift δt in our simulation is smaller than the width Δt; thus δt could be detected by the autocorrelation measurement for femtosecond laser pulse [62,63].

Note that one of the advantages of our protocol is the simultaneous measurement of Kerr rotation θ_k and Kerr ellipticity ε by selecting different postselected states. In Sec. II C, we discussed the reasons behind our choice of reselecting states $|\Psi_{f1}\rangle$ for θ_k measurement and $|\Psi_{f2}\rangle$ for ε measurement. These three criteria, namely, the sensitivity associated with the value of $\mathrm{Re}A_w/\mathrm{Im}A_w$, the monotonicity, and the minimum probability Π_w, were employed to determine the parameters $\gamma_{1,2}$ and $\eta_{1,2}$ for the postselected states $|\Psi_{f1,2}\rangle$. First, we find the appropriate postselections with sample $HfO_2(10\,\mathrm{nm})/Co(5\,\mathrm{nm})/HfO_2(30\,\mathrm{nm})/Al(40\,\mathrm{nm})/Si$ in Sec. IV A. Then, we further investigate the WVA enhancement for detecting the MOKE signals dependence of the thickness d of Co film in the cavity $HfO_2(10\,\mathrm{nm})/Co(5\,\mathrm{nm} < d < 50\,\mathrm{nm})/HfO_2(30\,\mathrm{nm})/Al(40\,\mathrm{nm})/Si$ in Sec. IV B. Finally, in Sec. IV C we demonstrate the advantage of WVA for MOKE detection in the cavity.

A. Postselection with sample $HfO_2(10\,\mathrm{nm})/Co(5\,\mathrm{nm})/HfO_2(30\,\mathrm{nm})/Al(40\,\mathrm{nm})/Si$

In this section, we first find the appropriate postselected states $|\Psi_{f1}\rangle$ for larger $\mathrm{Re}A_{w1}/\mathrm{Im}A_{w1}$ and $|\Psi_{f2}\rangle$ for smaller $\mathrm{Re}A_{w2}/\mathrm{Im}A_{w2}$, when detecting the Kerr signals with the sample $HfO_2(10\,\mathrm{nm})/Co(5\ \mathrm{nm})/HfO_2(30\ \mathrm{nm})/Al(40\,\mathrm{nm})/Si$ in the two MOKE geometries. Note that, in this sample, the thickness of the Co film does not change. Therefore, the monotonic relationship between the measured quantity and the result can be disregarded. In other words, we only need two conditions (the numerical results of $\mathrm{Re}A_w/\mathrm{Im}A_w$ and Π_w) to determine the values of γ and η. Through the calculation of the boundary matrix $\mathbf{A}_i$ and the transmission matrix $\mathbf{D}_i$ in the cavity, the Kerr rotation and the Kerr ellipticity in the polar geometry with the incident angle $\theta_0 = 80^\circ$ were obtained as $\theta_k^{(P)} = 1.0 \times 10^{-3}$ rad and $\varepsilon^{(P)} = 1.4 \times 10^{-3}$ rad. Similarly, the simulation results of Kerr signals in the longitudinal geometry with $\theta_0 = 3^\circ$ were obtained as $\theta_k^{(L)} = -2.8 \times 10^{-4}$ rad and $\varepsilon^{(L)} = -2.5 \times 10^{-4}$ rad. Subsequently, we calculate the dependence of value log $(\mathrm{Re}A_w/\mathrm{Im}A_w)$ on different postselected states at the parameters η-γ space in Fig. 5. The values of A_w at the range of $-0.004\,\mathrm{rad} < \eta < 0.004$ rad with different γ for the two MOKE geometries are shown in Fig. 6. Finally, we find the appropriate postselected states from Table I.

Note that the postselected state $|\Psi_f\rangle$ should be chosen to avoid falling below the detection threshold by compensating with a A_w while still guaranteeing the monotonicity; thereinto the monotonicity depends on the measured parameter θ_K or ε and the choice of $|\Psi_f\rangle$. For simultaneously measuring θ_K and ε, $|\Psi_{f1}\rangle$ for the amplification of θ_K needs to be prepared with the condition $\mathrm{Re}A_{w1}/\mathrm{Im}A_{w1} \gg 1$, while $|\Psi_{f2}\rangle$ for the amplification of ε needs to be prepared with $\mathrm{Re}A_{w1}/\mathrm{Im}A_{w1} \ll 1$. Figures 5(a) and 5(b) present the

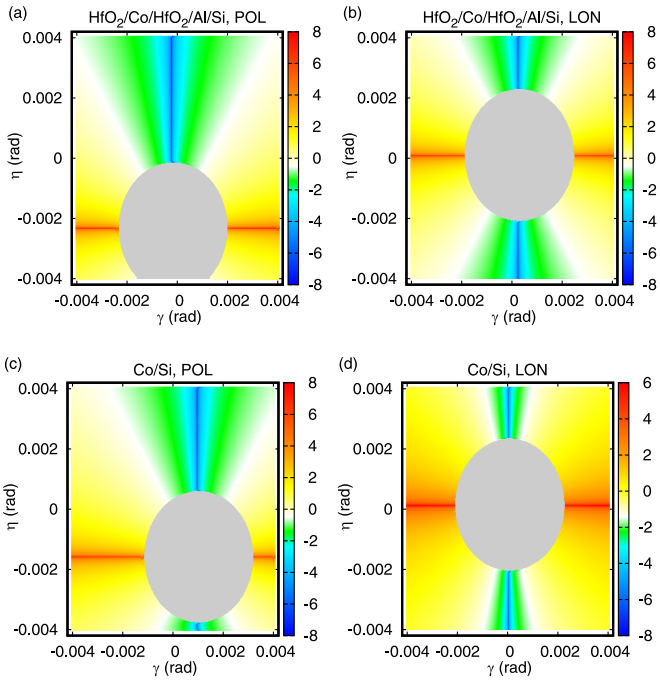

FIG. 5. The dependence of the value log $(\mathrm{Re}A_w/\mathrm{Im}A_w)$ on different postselected states in the parameters η-γ space, where γ represents the polarization angle of P2 and P3. Parameter η represents the phase difference induced by SBC1 and SBC2. (a) and (b) show the results with the sample $HfO_2(10\,\mathrm{nm})/Co(5\,\mathrm{nm})/HfO_2(30\,\mathrm{nm})/Al(40\,\mathrm{nm})/Si$ films. [(c), (d)] show the results with the sample Co(d nm)/Si films. The color-coded quantity is the value of log $(\mathrm{Re}A_w/\mathrm{Im}A_w)$. The gray ellipse represents WVA failing to detect signals.

dependence of log $(\mathrm{Re}A_w/\mathrm{Im}A_w)$ on different postselected states in the two geometries. It is intuitive and convenient to select $|\Psi_{f1,f2}\rangle$ for larger $\mathrm{Re}A_{w1}/\mathrm{Im}A_{w1}$ in the time domain and for smaller $\mathrm{Re}A_{w2}/\mathrm{Im}A_{w2}$ in the frequency domain from Fig. 5. Figure 6 shows the weak value at the range of $-0.004\,\mathrm{rad} < \eta < 0.004$ rad with $\gamma = -0.002$ rad (upper panels), $\gamma = 0.000$ rad (middle panels), and $\gamma = 0.002$ rad (lower panels) for the polar geometry (left panels) and for the longitudinal geometry (right panels). Table I displays the parameters and some characteristic numerical results from Fig. 6. The results indicate that the complex weak value $\mathrm{Re}A_w + i\mathrm{Im}A_w$ strongly depends on η and γ. It can be found that the measurement with state $|\Psi_{f0}\rangle$ is difficult to achieve because of the low probability Π_{w0} of successful post-selection. Therefore, states $|\Psi_{f1}\rangle$ and $|\Psi_{f2}\rangle$ need to be reselected. In the polar geometry, $|\Psi_{f1}^b\rangle^{(P)}$ is selected to obtain the amplification coefficient $\mathrm{Re}A_{w1} = 452$ with $\mathrm{Re}A_{w1}/\mathrm{Im}A_{w1} = 6.84$, while $|\Psi_{f2}\rangle$ is chosen at $|\Psi_{f2}^a\rangle^{(P)}$ for obtaining the amplification coefficient of $\mathrm{Im}A_{w2} = 429$ with $\mathrm{Re}A_{w2}/\mathrm{Im}A_{w2} = 0.07$ from Table I. Meanwhile, in the longitudinal geometry, we choose $|\Psi_{f1}^b\rangle^{(L)}$ in the time domain for obtaining $\mathrm{Re}A_{w1} = 433$ with $\mathrm{Re}A_{w1}/\mathrm{Im}A_{w1} = 24.0$, and we select $|\Psi_{f2}^a\rangle^{(L)}$ in the frequency domain for obtaining $\mathrm{Im}A_{w2} = 242$ with $\mathrm{Re}A_{w2}/\mathrm{Im}A_{w2} = 0.07$. Note that the choice of postselected state $|\Psi_f\rangle$ in Table I is constrained by the minimum step size of the polarizers and the SBCs. Therefore, when we exceed the limitations of η and

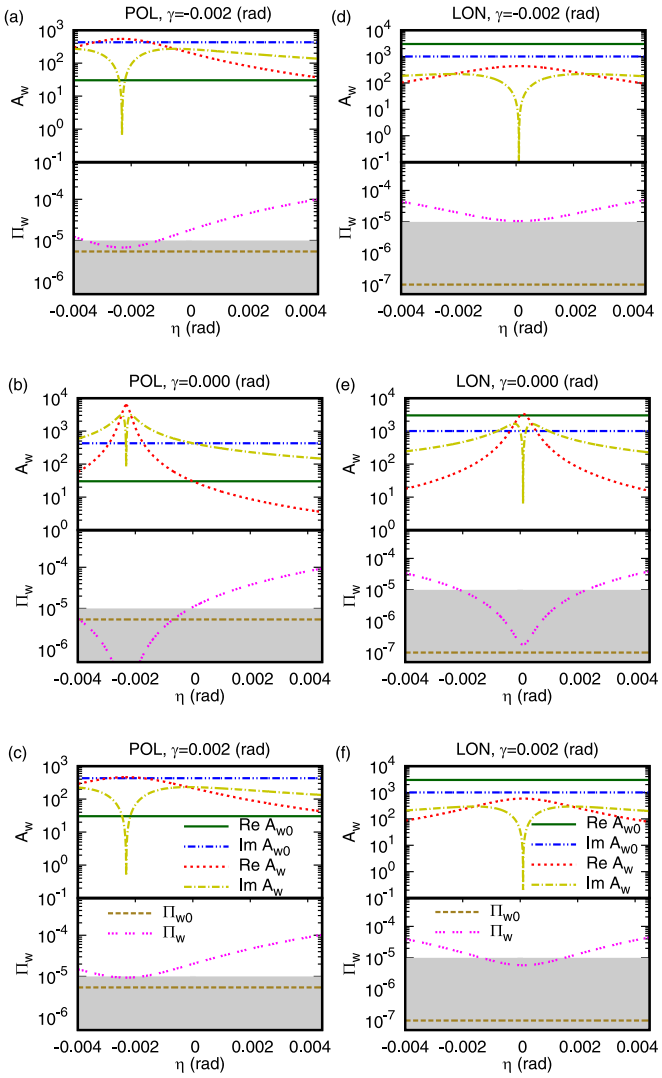

FIG. 6. Comparison of various postselections in the polar geometry (left panels) and in the longitudinal geometry (right panels) for detecting the MOKE on the nanoscale layered structure of $HfO_2(10\,nm)/Co(5\,nm)/HfO_2(30\,nm)/Al(40\,nm)/Si$ films. Here, the polar MOKE signal $\theta_k + i\varepsilon = (0.2 + i2.3) \times 10^{-3}$ rad are measured with incident angle $\theta_0 = 80^\circ$. The longitudinal MOKE signal $\theta_k + i\varepsilon = (-0.29 - i0.1) \times 10^{-3}$ rad are measured with incident angle $\theta_0 = 3^\circ$. The gray band represents the weak measurement failing to detect the final signal.

γ, more suitable postselected states $|\Psi^f\rangle$ can be identified, as demonstrated in Fig. 5.

In principle, an effective measurement must be such that the function between the parameter of interest and the measured result is monotonic at a certain measurement range. Therefore, the limit of the monotonic relationship between the measured quantity (corresponding to the MOKE signals) and the result (A_w) needs to be further investigated. Meanwhile, the postselected state $|\Psi_f\rangle$ needs to be chosen more strictly when the thickness of Co changes in a nanoscale layered structure, and the detail will be discussed in the next section.

TABLE I. Characteristic parameters and results (dimensional quantities in a unit of 10^{-3} rad) in the polar (POL) geometry and the longitudinal (LON) geometry using the sample $HfO_2(10\,nm)/Co(5\,nm)/HfO_2(30\,nm)/Al(40\,nm)/Si$. The Kerr angle is calculated as $\theta_k + i\varepsilon = (0.2 + i2.3) \times 10^{-3}$ rad for the POL geometry and $\theta_k + i\varepsilon = (-0.29 - i0.1) \times 10^{-3}$ rad for the LON geometry.

	$\|\Psi_f\rangle$	γ	η	A_w	$\frac{\mathrm{Re}A_w}{\mathrm{Im}A_w}$	$\log(\Pi_w)$
POL	$\|\Psi_{f0}\rangle^{(P)}$	0	0	$0.30 \times 10^2 + 4.29 \times 10^2 i$	0.06	−5.2
	$\|\Psi^a_{f1}\rangle^{(P)}$	2	−3	$4.20 \times 10^2 + 1.32 \times 10^2 i$	3.18	−4.9
	$\|\Psi^b_{f1}\rangle^{(P)}$	2	−2	$4.52 \times 10^2 + 0.66 \times 10^2 i$	6.84	−5.0
	$\|\Psi^c_{f1}\rangle^{(P)}$	2	−1	$3.37 \times 10^2 + 2.05 \times 10^2 i$	1.64	−4.9
	$\|\Psi^a_{f2}\rangle^{(P)}$	0	0	$0.30 \times 10^2 + 4.29 \times 10^2 i$	0.07	−4.9
	$\|\Psi^b_{f2}\rangle^{(P)}$	0	1	$0.14 \times 10^2 + 3.00 \times 10^2 i$	0.05	−4.6
	$\|\Psi^c_{f2}\rangle^{(P)}$	0	2	$0.08 \times 10^2 + 2.31 \times 10^2 i$	0.03	−4.4
LON	$\|\Psi_{f0}\rangle^{(L)}$	0	0	$2.99 \times 10^3 + 1.00 \times 10^3 i$	2.99	−6.9
	$\|\Psi^a_{f1}\rangle^{(L)}$	−2	−1	$3.53 \times 10^2 + 1.69 \times 10^2 i$	2.08	−5.0
	$\|\Psi^b_{f1}\rangle^{(L)}$	−2	0	$4.33 \times 10^2 + 0.18 \times 10^2 i$	24.0	−4.9
	$\|\Psi^c_{f1}\rangle^{(L)}$	−2	1	$3.77 \times 10^2 + 1.47 \times 10^2 i$	2.56	−4.9
	$\|\Psi^a_{f2}\rangle^{(L)}$	0	−4	$0.17 \times 10^2 + 2.42 \times 10^2 i$	0.07	−4.5
	$\|\Psi^b_{f2}\rangle^{(L)}$	0	−3	$0.31 \times 10^2 + 3.19 \times 10^2 i$	0.09	−4.7
	$\|\Psi^c_{f2}\rangle^{(L)}$	0	−2	$0.66 \times 10^2 + 4.66 \times 10^2 i$	0.14	−5.0

B. Application for measuring the thickness of Co in nanoscale layered structure

The ability to detect changes in the thickness of a MO object allows the investigation of the geometry and topology of two-dimensional patterned planar single- or multi-layered magnetic structures. This is particularly relevant when the thickness of these structures is on the order of a characteristic magnetic lengthscale [1,10]. Due to the advantage of the high sensitivity, down to a thickness of an atomic layer, the MOKE technique may also have the potential to explore more complex and valuable magnetic phenomena in three-dimensional nanomagnetism. Therefore, we further investigate the dependence of WVA enhancement on the Co thickness in the range $5\,nm < d < 50\,nm$ using the sample $HfO_2(10\,nm)/Co(d\,nm)/HfO_2$ $(30nm)/Al(40\,nm)/Si$ for two MOKE geometries. In contrast to the previous subsection, where we studied the sample $HfO_2(10\,nm)/Co(5\,nm)/HfO_2(30\,nm)/Al(40\,nm)/Si$, we now need to consider the limit of the monotonic relationship between the measured quantity (corresponding to the thickness as well as the MOKE signals) and the result (A_w).

Figure 7 displays the dependence of pointer shift and its sensitivity on the thickness d for detecting the sample $HfO_2(10\,nm)/Co(d\,nm)/HfO_2(30\,nm)/Al(40\,nm)/Si$ films in the two MOKE geometries. The sensitivities $\delta t/\delta d$ and $\delta\lambda/\delta d$ in Fig. 7(c) and Fig. 7(f) can better represent the monotony at the certain measurement range, where the curves marked with "$+|\Psi_f\rangle$" represent the positive value of sensitivity, and the curves marked with "$-|\Psi_f\rangle$" represent the negative value of sensitivity. In principle, the sign of the sensitivity should be constant over the entire measurement range.

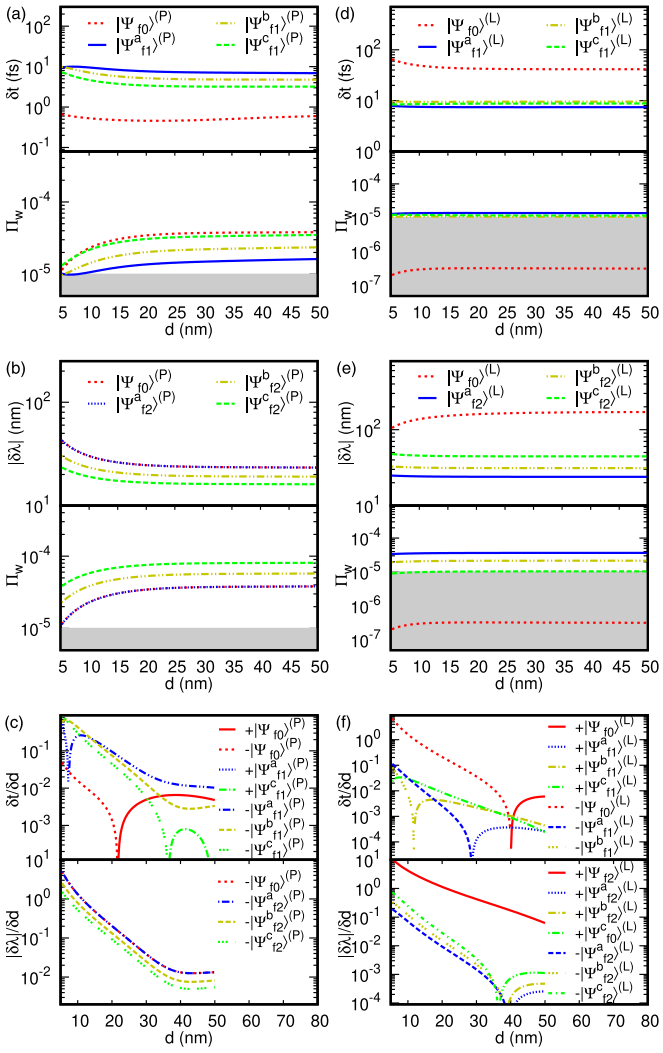

FIG. 7. The pointer shift and its sensitivity for detecting the sample $HfO_2(10\,\text{nm})/Co(d\,\text{nm})/HfO_2(30\,\text{nm})/Al(40\,\text{nm})/Si$ in the polar geometry (left panels) and in the longitudinal geometry (right panels). [(a),(d)] The time shift with the corresponding probability Π_w. [(b),(e)] The wavelength shift with the corresponding probability Π_w. [(c),(f)] The sensitivities $\delta t/\delta d$ and $\delta\lambda/\delta d$ for the measurements in the time and frequency domains.

For the polar geometry, the results indicate that $\delta t(d)$ and $\delta\lambda(d)$ with various $|\Psi_f\rangle$ are not all monotonic at the measurement range $5\,\text{nm} < d < 50$ nm. Therefore, after considering the monotonic relationship between the pointer shifts and the thickness of Co film, only $|\Psi^b_{f1}\rangle^{(P)}$ can be selected for detecting δt. For the $\delta\lambda$ measurement in the frequency domain, all states $|\Psi_{f2}\rangle^{(P)}$ can be used for the WVA measurement. In addition, the probability Π_w in Fig. 7(b) and the sensitivity $\delta\lambda/\delta d$ in Fig. 7(c) indicate the inherent dilemma of the WVA measurement: a higher sensitivity is obtained at the cost of the reduced the probability Π_w and the lower signal-to-noise ratio (SNR) [64]. Thus, the choice of the actual state $|\Psi_{f2}\rangle^{(P)}$ depends on whether our measurement conditions depend more on the sensitivity or SNR.

For the longitudinal geometry, similar results can be obtained from the right panels of Fig. 7. When detecting the temporal shift δt, only the postselected state $|\Psi^c_{f1}\rangle^{(L)}$ can be chosen. For detecting the momentum shift $\delta\lambda$, the results in Fig. 7(f) indicate that the curves of $\delta\lambda$ with all states are not monotonous in the range of $5\,\text{nm} < d < 50$ nm. Note that the previous discussion in Sec. IV A indicates that all states $|\Psi^a_{f2}\rangle^{(L)}$, $|\Psi^b_{f2}\rangle^{(L)}$, and $|\Psi^c_{f2}\rangle^{(L)}$ are suitable for the measurement of the cavity with a determined thickness of Co film; however, these states lead to the non-monotonicity of the $\delta\lambda(d)$ measurement and fail to detect the thickness d at the range of $5\,\text{nm} < d < 50$ nm. At the very least, if we relax the measurement conditions, for example, reduce the measurement range to $5\,\text{nm} < d < 35$ nm, all states $|\Psi^a_{f2}\rangle^{(L)}$, $|\Psi^b_{f2}\rangle^{(L)}$, and $|\Psi^c_{f2}\rangle^{(L)}$ can be used for the $\delta\lambda(d)$ measurement in the range of $5\,\text{nm} < d < 35$ nm. Our results suggest that the postselection states should be selected more carefully when considering the monotonic relationship.

C. Enhancement of the cavity and WVA

In this study, we present the results of combining the cavity and WVA techniques, as depicted in Fig. 7. Our aim is to ascertain the contributions of WVA and the cavity in inducing time or wavelength shifts with varying Co thickness. Additionally, we investigate the potential of WVA to enhance Kerr signals in conjunction with the cavity, particularly when the cavity alone fails to produce significant enhancement. To demonstrate the amplification capabilities of WVA in the cavity setup, we implement four distinct schemes for detecting Kerr signals as a function of the Co film thickness. The reasons for selecting the four schemes are outlined as follows.

(1) TMOKES + Single: This scheme represents the traditional MOKE setup with a single Co film. It serves as the simplest approach for detecting MOKE signals and can be used as a benchmark for comparing results obtained from different schemes.

(2) TMOKES + Cavity: This scheme involves the traditional MOKE setup with a cavity. While constructing a multilayer cavity can effectively enhance the MOKE signal of magnetic films for both theoretical investigations and practical applications [17–19,65], the degree of enhancement strongly depends on the wavelength and thickness of the MO subjects. Therefore, this paper focuses on scenarios where a multilayer cavity fails to amplify the MOKE signals, as depicted in Fig. 8(c).

(3) WVA + Single: This scheme involves WVA measurement using a single Co film. It was studied with simple samples in previous work [39–41]. Note that there is a difference between the WVA pointers used in their work and the ones in this paper. In previous studies, the pointer with the transversal profile is employed to detect transversal shift, whereas in this work, we employ the standard WVA approach [23] to detect longitudinal temporal and frequency shifts. The primary motivation for selecting the longitudinal pointer in this paper is its ability to exhibit longitudinal shifts in both the time domain and the frequency domain while utilizing a Fourier-limited Gaussian pulse. We further investigate the enhancement of longitudinal shifts using the standard WVA approach, comparing it with the TMOKES schemes.

(4) WVA + Cavity: This scheme involves WVA measurement in conjunction with a cavity. The primary objective of

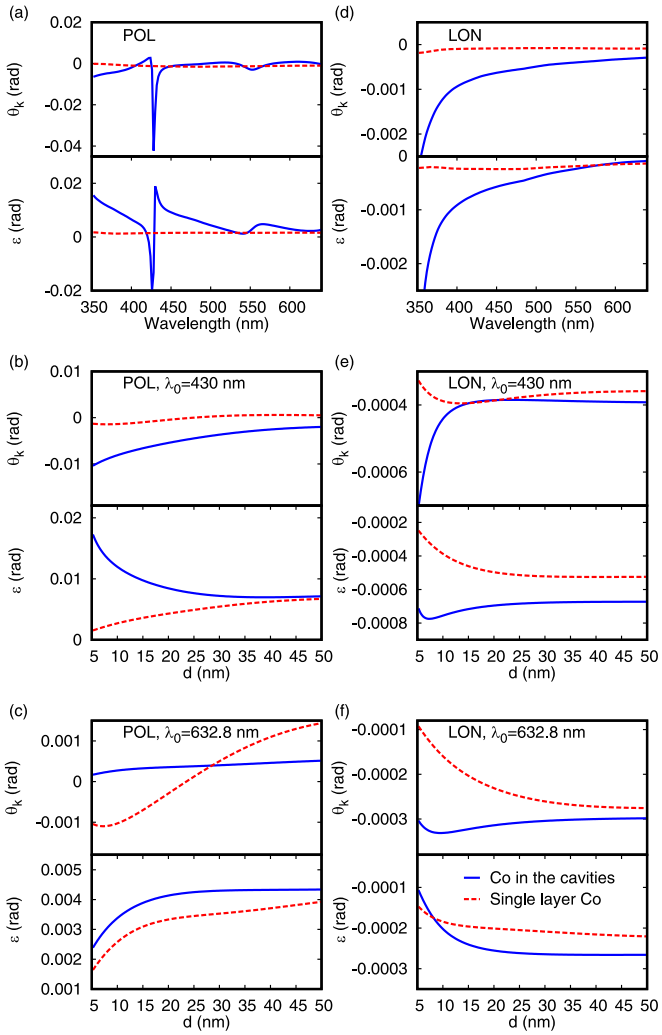

FIG. 8. Comparison of the results of the Kerr rotation θ_k and the Kerr ellipticity ϵ in the schemes "TWVA + Cavity" (blue curves) and "TWVA + Single" (red curves). [(a),(d)] The dependence of the Kerr signals on the wavelength. [(b),(e)] The dependence of the Kerr signals on thickness d when $\lambda_0 = 430$ nm. [(c),(f)] The dependence of the Kerr signals on thickness d when $\lambda_0 = 632.8$ nm.

this paper is to explore the capability of WVA to enhance Kerr signals simultaneously with the cavity, particularly in cases where the cavity alone fails to produce significant enhancement. In other words, we aim to determine whether WVA has the potential to enhance the MOKE signals irrespective of the sample structures and MOKE geometry.

We calculate the results of "TMOKES + Single" and "TMOKES + Cavity" by the traditional MOKE approach in Sec. III. The dependency of ratios on the thickness d is shown in Fig. 11. The results of "WVA + Cavity" are shown in Sec. IV B. In Sec. IV C 1, we compare the Kerr signals between "TMOKES + Single" and "TMOKES + Cavity" by calculating the Kerr signals for the samples consisting of Co(d nm)/Si films, as well as the cavity configuration HfO_2(10 nm)/Co(d nm)/HfO_2(30 nm)/Al(40 nm)/Si films. Moreover, in Sec. IV C 2, we present the results of "WVA + Single" obtained by applying the WVA measurement on the samples with Co(5 nm)/Si films. Lastly, in Sec. IV C 3, we summarize the advantages of the WVA technique within the cavity setup.

1. *MOKE enhancement of the cavity without WVA*

To compare "TMOKES + Single" and "TMOKES + Cavity" schemes and highlight the enhancement of the cavity without WVA, the Kerr singles with the sample HfO_2(10 nm)/Co(d nm)/HfO_2(30 nm)/Al(40 nm)/Si films and the sample Co(d nm)/Si films are calculated and displayed in Fig. 8. In addition, the measurement results of ratios $I_1^{\theta_k}/I_2^{\theta_k}$ and $I_2^{\varepsilon}/I_1^{\varepsilon}$ are shown in Fig. 11.

Figure 8 demonstrates the Kerr rotation θ_k and the Kerr ellipticity ε enhancement with the two samples as a function of the wavelength of incidence of the light and as a function of the thickness d of Co. Figures 8(a) and 8(d) confirm that the cavity can effectively enhance both θ_k and ε. The results also indicate that the enhancement strongly depends on the wavelength. For the measurement in the longitudinal geometry, the dependency is clear and the enhancement increase as the wavelength decreases. For the measurement in the polar geometry, the amplification of θ_k is strongest at wavelengths of 430 nm, and the peaks of ε appear at the wavelength of 425 nm and at the wavelength of 430 nm. Note that there are changes in θ_k sign and ε sign in Fig. 8(a) with the cavity. Similarly, the change of the Kerr rotation sign also can be obtained as a function of the wavelength of the incident light in the HfO_2/Co/HfO_2/Al/Si structure [17]. And this change is due to the phase shift of the Fresnel reflection coefficient of the multilayer structure jumping about π in the wavelength region [66].

To investigate the dependence of Kerr signals on the thickness d at a certain wavelength λ, it can be found in Fig. 8(b) and Fig. 8(e) that the bigger Kerr signals in the two geometries can be obtained with the cavity at the wavelength of 430 nm. Furthermore, the enhancement decreases as the thickness d of Co film increases. When the incident light is set at a wavelength of 632.8 nm, Figs. 8(c) and 8(f) indicate that Kerr signals with the cavity are not always greater than Kerr signals with the sample Co(d nm)/Si films in the range of 5 nm $< d <$ 50 nm. Specifically, Kerr rotation θ_k with the cavity is smaller than that with the sample Co(d nm)/Si films in the range of 30 nm $< d <$ 50 nm. Note that this is the situation when the cavity fails to amplify the MOKE signals and one of the reasons why we investigate WVA for further enhancing the MOKE signals in this case.

2. *WVA for MOKE detection with the sample Co(d nm)*

Following the study of "WVA + Cavity", the results of "WVA + Single" by applying the WVA measurement with the sample Co(5 nm)/Si films are simulated. First, the dependence of value log (ReA_w/ImA_w) on different postselected states are shown in Figs. 5(c) and 5(d). Then, the appropriate postselected state for WVA with the sample Co(5 nm)/Si films is selected and displayed in Table II. Finally, the dependence of pointer shift and its sensitivity on the thickness d are shown in Fig. 9. These states are remarked as $|\Upsilon_f\rangle$ to distinguish this state from the symbol $|\Psi_f\rangle$ in the scheme "WVA + Cavity". By considering the larger ReA_{w1}/ImA_{w1} and the smaller ReA_{w2}/ImA_{w2}, the detectability as well as the

TABLE II. Characteristic parameters and results (dimensional quantities in a unit of 10^{-3} rad) in the polar (POL) geometry and the longitudinal (LON) geometry using the sample Co(5 nm). The Kerr angle is calculated as $\theta_k + i\varepsilon = (0.2 + i1.9) \times 10^{-3}$ rad for the POL geometry and $\theta_k + i\varepsilon = (0.087 - i0.13) \times 10^{-3}$ rad for the LON geometry.

	$\lvert\Upsilon_f\rangle$	γ	η	A_w	$\frac{\mathrm{Re}A_w}{\mathrm{Im}A_w}$	$\log(\Pi_w)$
	$\lvert\Upsilon_{f0}\rangle^{(P)}$	0	0	$2.89 \times 10^2 + 4.44 \times 10^2 i$	0.65	−5.4
	$\lvert\Upsilon^a_{f1}\rangle^{(P)}$	−2	−3	$2.70 \times 10^2 + 1.26 \times 10^2 i$	2.14	−4.6
	$\lvert\Upsilon^b_{f1}\rangle^{(P)}$	−2	−2	$3.23 \times 10^2 + 0.48 \times 10^2 i$	6.72	−4.7
POL	$\lvert\Upsilon^c_{f1}\rangle^{(P)}$	−2	−1	$3.18 \times 10^2 + 0.61 \times 10^2 i$	5.21	−4.7
	$\lvert\Upsilon^a_{f2}\rangle^{(P)}$	0	1	$1.33 \times 10^2 + 3.34 \times 10^3 i$	0.39	−4.8
	$\lvert\Upsilon^b_{f2}\rangle^{(P)}$	0	2	$0.74 \times 10^2 + 2.57 \times 10^2 i$	0.28	−4.5
	$\lvert\Upsilon^c_{f2}\rangle^{(P)}$	0	3	$0.46 \times 10^2 + 2.07 \times 10^2 i$	0.22	−4.3
	$\lvert\Upsilon_{f0}\rangle^{(L)}$	0	0	$3.09 \times 10^3 + 5.03 \times 10^3 i$	5.50	−7.5
	$\lvert\Upsilon^a_{f1}\rangle^{(L)}$	−4	−1	$2.26 \times 10^2 + 0.63 \times 10^2 i$	3.58	−4.4
	$\lvert\Upsilon^b_{f1}\rangle^{(L)}$	−4	0	$2.44 \times 10^2 + 0.08 \times 10^2 i$	30.5	−4.4
	$\lvert\Upsilon^c_{f1}\rangle^{(L)}$	−4	1	$2.34 \times 10^1 + 0.49 \times 10^2 i$	4.77	−4.4
LON	$\lvert\Upsilon^a_{f2}\rangle^{(L)}$	0	−4	$0.05 \times 10^2 + 2.41 \times 10^2 i$	0.02	−4.4
	$\lvert\Upsilon^b_{f2}\rangle^{(L)}$	0	−3	$0.08 \times 10^1 + 3.17 \times 10^2 i$	0.03	−4.7
	$\lvert\Upsilon^c_{f2}\rangle^{(L)}$	0	−2	$0.19 \times 10^0 + 4.65 \times 10^2 i$	0.02	−5.0

monotonicity, the states $|\Upsilon^c_{f1}\rangle^{(P)}$, $|\Upsilon^a_{f2}\rangle^{(P)}$, $|\Upsilon^c_{f1}\rangle^{(L)}$, and $|\Upsilon^c_{f2}\rangle^{(L)}$ are selected for the "WVA + Cavity" measurement in the range of 5 nm $< d <$ 50 nm. These states are also chosen by finding the largest δt for amplifying Kerr rotation and the largest $\delta\lambda$ for amplifying Kerr ellipticity as we discussed in Sec. IV A.

3. *Advantage of the WVA technique*

Finally, we investigate the advantage of WVA by comparing the results with different schemes. Figure 10 shows the pointer shifts and their sensitivities in the schemes "WVA + Cavity" and "WVA + Single" at the most appropriate postselected state, where the most appropriate states $|\Psi_f\rangle$ and $|\Upsilon_f\rangle$ are chosen with the standards of satisfying the detectability, the monotonicity, the larger $\mathrm{Re}A_{w1}/\mathrm{Im}A_{w1}$ for amplifying Kerr rotation and the smaller $\mathrm{Re}A_{w2}/\mathrm{Im}A_{w2}$ for amplifying Kerr ellipticity, and the highest sensitivity. In addition, Fig. 11 displays the measurement of Kerr signals dependency of the thickness d in the four schemes. Several conclusions can be obtained.

(i) For the temporal shift measurement in the polar geometry, Fig. 10(a) indicates that δt with the cavity is bigger than shift δt with the sample Co(d nm)/Si films. However, Fig. 10(c) shows that the sensitivity $\delta t/\delta d$ with the cavity is lower than $\delta t/\delta d$ with the sample Co(d nm)/Si films in the range of 20 nm $< d <$ 50 nm. Meanwhile, Kerr rotation θ_k with the cavity is smaller than that with the sample Co(d nm)/Si films in the range of 30 nm $< d <$ 50 nm. The same conclusion can also be found from Fig. 11(a). Therefore, the fact that δt with the cavity being larger than shift δt with the sample Co(d nm)/Si demonstrates that WVA can efficiently enhance θ_k, especially when the cavity can not efficiently enhance the Kerr rotation θ_k.

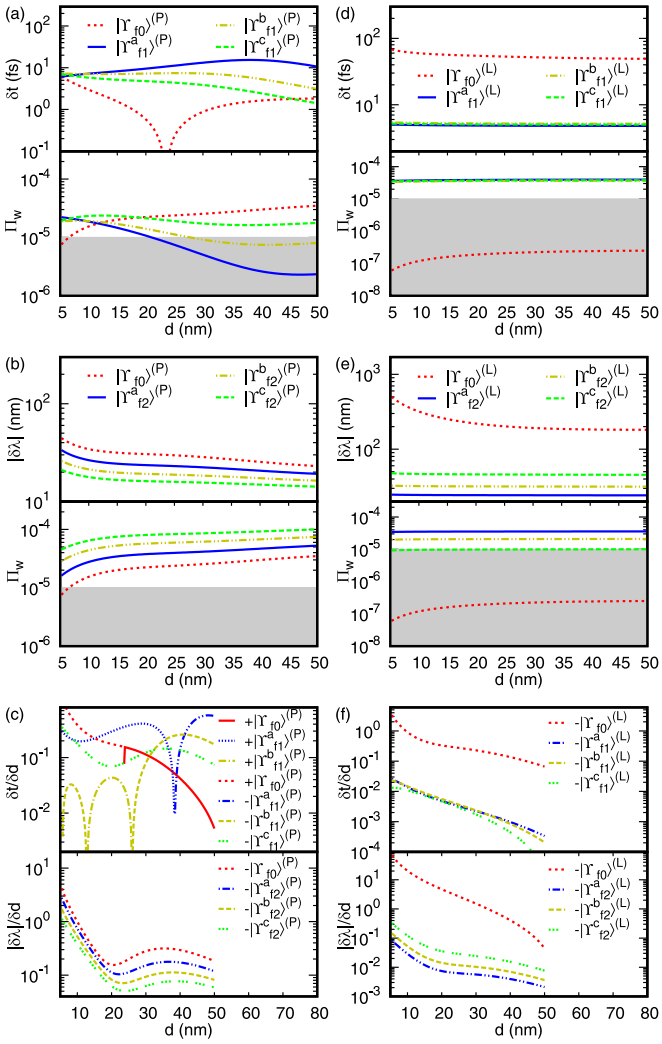

FIG. 9. The dependence of pointer shift and its sensitivity on the thickness d for detecting the sample Co(d nm). [(a),(d)] The time shift with the corresponding probability Π_w. [(b),(e)] The wavelength shift with the corresponding probability Π_w. [(c),(f)] The sensitivity $\delta t/\delta d$ for the time shift measurement and the sensitivity $\delta\lambda/\delta d$ for the spectral shift measurement.

(ii) For the wavelength shift measurement in the polar geometry, Fig. 10(b) shows that $\delta\lambda$ with the cavity is larger than the shift $\delta\lambda$ with the sample Co(d nm)/Si. In addition, as shown in Fig. 10(b), Kerr ellipticity ε with the cavity is also larger than that with the sample Co(d nm)/Si in the range of 5 nm $< d <$ 50 nm. So, both the cavity and WVA can enhance Kerr ellipticity ε in the polar geometry.

(iii) In Fig. 10(c), both the curves of $\delta t/\delta d$ and $\delta\lambda/\delta d$ with different samples intersect each other. However, $\delta t/\delta d$ and $\delta\lambda/\delta d$ with the cavity are higher than that with the sample Co(d nm)/Si films at the smaller measurement range, such as 5 nm $< d <$ 20 nm. Therefore, the combination of WVA and the cavity can obtain higher sensitivity than the WVA measurement with the sample Co(d nm)/Si films in the range of 5 nm $< d <$ 20 nm.

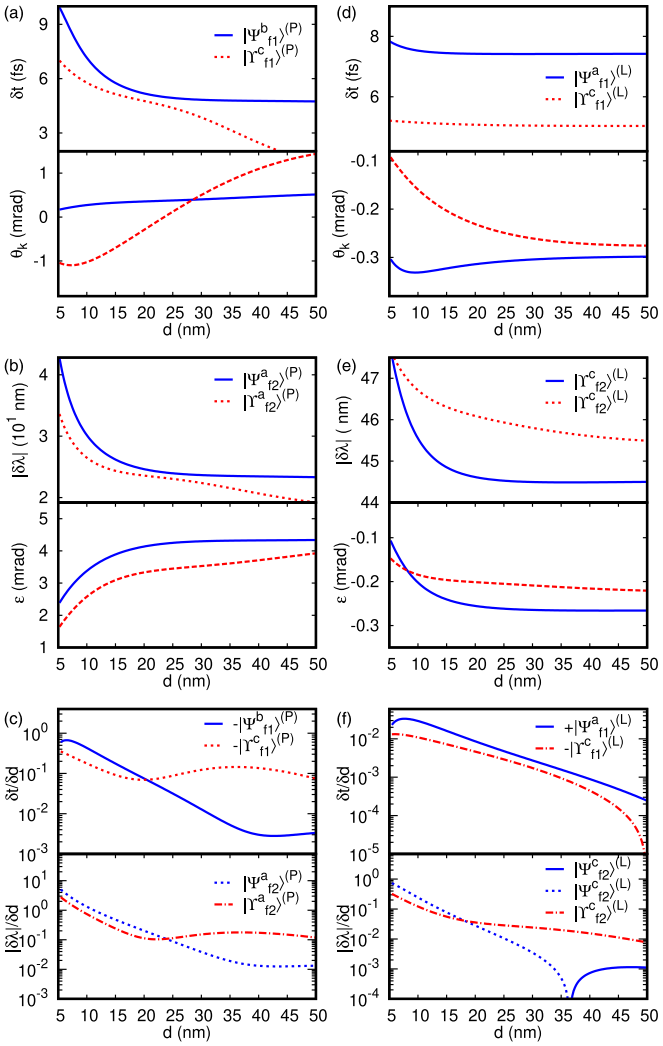

FIG. 10. Comparison of the schemes "WVA + Cavity" (blue curves) and "WVA + Single" (red curves). [(a),(c)] The dependence of time shift and the Kerr rotation θ_k on thickness d. [(b),(e)] The dependence of wavelength shift and the Kerr ellipticity ϵ on thickness d. [(c),(f)] The dependence of sensitivities $\delta t/\delta d$ and $\delta\lambda/\delta d$ on thickness d.

(iv) For the temporal shift measurement in the longitudinal geometry, both the temporal shift δt in Fig. 10(d) and its sensitivity in Fig. 10(f) show that δt and $\delta t/\delta d$ with the combination of WVA and the cavity are larger than that with the application of WVA on sample Co(d nm)/Si films in the range of 5 nm $< d <$ 50 nm.

(v) For the frequency shift measurement in the longitudinal geometry, it can be found in Fig. 10(e) that $\delta\lambda$ with the cavity is smaller than the shift with the sample Co(d nm)/Si films in the range of 5 nm $< d <$ 50 nm. However, the sensitivity $\delta\lambda/\delta d$ with the cavity is larger than $\delta\lambda/\delta d$ with the sample Co(d nm)/Si films in the range of 5 nm $< d <$ 15 nm. Meanwhile, Figs. 10(e) and 10(f) indicate that the cavity may contribute very little to WVA for the frequency shift measurement in the longitudinal geometry. However, the combination of WVA and the cavity still shows its advantages over the application of WVA on sample Co(d nm)/Si films with higher sensitivity in the range of 5 nm $< d <$ 15 nm.

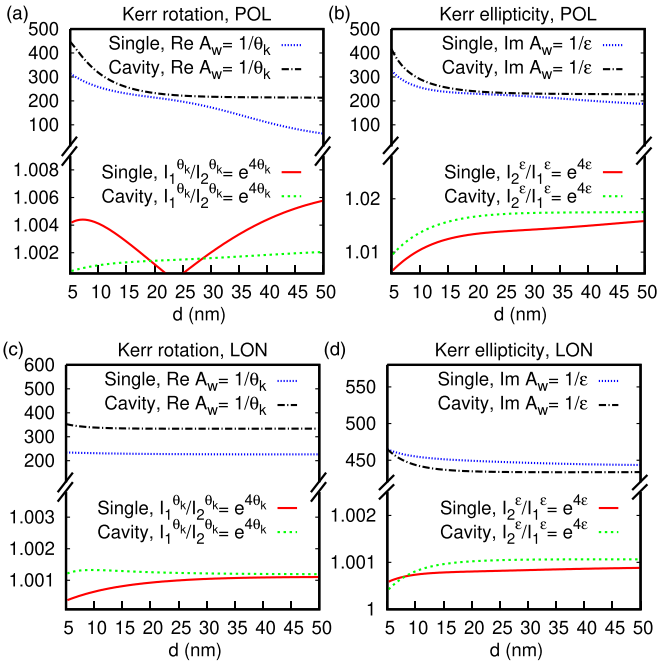

FIG. 11. The measurement of Kerr rotation θ_k and Kerr ellipticity ε in the four schemes of "TMOKES + Single" (red curves), "TMOKES + Cavity" (green curves), "WVA + Single" (blue curves) and "WVA + Cavity" (black curves). [(a),(c)] The measurement of the Kerr rotation θ_k; [(b),(d)] the measurement of the Kerr ellipticity ε.

(vi) Figures 10(a), 10(b), 10(d), and 10(e) show that the pointer shift δt and $\delta\lambda$ are inversely proportional to Kerr rotation θ_k and Kerr ellipticity ε, respectively, which are consistent with the analysis in Eqs. (15) and (16). The smaller Kerr signals lead to larger pointer shifts. Therefore, the amplification of Kerr signals is more significant when the signals become smaller. In addition, Fig. 11 indicates that the cavity contributes very little to the scheme "WVA + Cavity" and WVA shows a great advantage in amplifying the Kerr signals over the TMOKES scheme regardless of the structures of the sample and the MOKE geometries.

Based on the above discussion, we conclude that WVA can effectively enhance the Kerr signals in two cases: First, the combination of the cavity and WVA in "WVA + Cavity" can further enhance the MOKE signals, when compared to the measurement of directly applying WVA to detect the MOKE signals with the sample Co(d nm)/Si films in "WVA + Single" and the enhancement in various cases is more prominent with higher sensitivities at a measurement range of 5 nm $< d <$ 15 nm. What's more, WVA can demonstrate the amplification of the MOKE signals, even when the cavity in "TMOKES + Cavity" fails to amplify the Kerr signals as shown in the conclusion (i) and in Fig. 11(a).

V. SUMMARY

In this paper, we investigated the application of WVA in detecting the MOKE in the nanoscale layered structure both in the longitudinal geometry and in the polar geometry.

The Kerr signals are set and amplified as the parameters in the "preselection" in WVA. The most sensitive relationship between Kerr signals and the pointer shift depends on finding the most appropriate post-selection state. We numerically model the dependence of the thickness of Co with the samples of both the nanoscale layered structure $HfO_2(10\,\mathrm{nm})/Co(d\,\mathrm{nm})/HfO_2(30\,\mathrm{nm})/Al(40\,\mathrm{nm})/Si$ films and the $Co(d\,\mathrm{nm})/Si$ films in the range of $5\,\mathrm{nm} < d < 50\,\mathrm{nm}$. The results indicated that the combination of the cavity and WVA can effectively and simultaneously amplify the MOKE signals when compared to the application of WVA on the sample $Co(d\,\mathrm{nm})$, and the enhancement in various cases is more prominent with higher sensitivities at a measurement range of $5\,\mathrm{nm} < d < 15\,\mathrm{nm}$, especially when the cavity shows no advantage for enhancing Kerr signals over the $Co(d\,\mathrm{nm})/Si$ films without WVA [see conclusion (i) and Fig. 11(a) in Sec. IV C 3].

Finally, we highlight the focus of this paper. (i) The limit of the monotonic relationship between the measured quantity and the result of the weak measurement is first investigated. It is constructive that the postselection should be chosen carefully to avoid the non-monotonicity (see the result of the state $|\Psi_{f2}^{b}\rangle$ in Fig. 7). (ii) Our protocol shows the advantage of simultaneously employing amplified temporal and momentum shifts to enhance Kerr signals by choosing different postselected states. (iii) WVA shows a great advantage in amplifying the Kerr signals over the TMOKES scheme regardless of the structures of the sample and the MOKE geometries. (iv) WVA still has the ability to enhance the MOKE signals, even when the cavity fails to amplify the Kerr signals. Therefore, WVA could potentially be used for studying the MO properties and the topology in more complicated nanoscale layered structures.

It is crucial to emphasize that our work aims to achieve simultaneous measurements of Kerr rotation θ_k and Kerr ellipticity ε while assuming a prior knowledge of the refractive index magnitude of the MO material. However, for a comprehensive MO characterization of any sample, the determination of at least four material constants becomes necessary, as exemplified in the application of generalized MO ellipsometry [67]. To enable the measurement of these four material constants using WVA, it is worthwhile to explore beyond the scope of this study by employing a more sophisticated pointer, such as the Hermite-Gaussian (HG) state [30,68,69], for multiparameter estimation. In addition, the comparison of this work to the lock-in detection technique for noise suppression has not been discussed [1]. Nevertheless, several existing studies highlighted the robustness of the standard WVA technique and its effectiveness in mitigating systematic errors [27,70,71].

In any WVA scheme, coupling the system to additional (unmeasured) pointers will lead to the effect of decoherence in the measured results, which reduces measurement precision. However, the use of a large imaginary weak value has been found to be particularly robust to decoherence [70]. Recent work has even shown that a WVA measurement using a mixture of coherent states can work better than using a single pure coherent state based on Fisher information analysis [72].

ACKNOWLEDGMENTS

This study was supported by the National Science Foundation of China (Grant No. 42220104002), the Canada Research Chairs (CRC) Program, the Canada First Research Excellence Fund (CFREF), and the Natural Sciences and Engineering Research Council (NSERC). A.C.D. acknowledges support from the EPSRC, Impact Acceleration Account (Grant No. EP/R511705/1). J.-H.H. Huang acknowledges support from the China Scholarship Council (Grant No. 202206410063).

APPENDIX A: EXPRESSION OF THE BOUNDARY MATRIX AND THE TRANSMISSION MATRIX

The transmission 4×4 matrix $\mathbf{D}$ relates the s and p components of the electric field at two surfaces of a film of thickness d [1]. Based upon a generalization of the formalism of Zak *et al.* [43,73], the boundary matrix $\mathbf{A}$ and the transmission matrix $\mathbf{D}$ for both the longitudinal (L) case and polar (P) case can be provided as

$$\mathbf{A}^{(\mathrm{P})} = \begin{pmatrix} 1 & 0 & 1 & 0 \\ \frac{i}{2}\alpha_y^2 Q & \alpha_z & \frac{i}{2}\alpha_y^2 Q & -\alpha_z \\ \frac{i}{2}\alpha_z QN & -N & -\frac{i}{2}\alpha_z QN & -N \\ \alpha_z N & \frac{i}{2}QN & -\alpha_z N & \frac{i}{2}QN \end{pmatrix}, \tag{A1}$$

$$\mathbf{A}^{(\mathrm{L})} = \begin{pmatrix} 1 & 0 & 1 & 0 \\ -m_z Q & \alpha_z & m_z Q & -\alpha_z \\ \frac{i}{2}\alpha_y QN & -N & \frac{i}{2}\alpha_y QN & -N \\ \alpha_z N & n_z QN & -\alpha_z N & -n_z QN \end{pmatrix}, \tag{A2}$$

$$\mathbf{D}^{(\mathrm{P})} = \begin{pmatrix} U\cos\sigma^P & U\sin\sigma^P & 0 & 0 \\ -U\sin\sigma^P & U\cos\sigma^P & 0 & 0 \\ 0 & 0 & \frac{\cos\sigma^P}{U} & \frac{\sin\sigma^P}{U} \\ 0 & 0 & -\frac{\sin\sigma^P}{U} & \frac{\cos\sigma^P}{U} \end{pmatrix}, \tag{A3}$$

$$\mathbf{D}^{(\mathrm{L})} = \begin{pmatrix} U\cos\sigma^L & U\sin\sigma^L & 0 & 0 \\ -U\sin\sigma^L & U\cos\sigma^L & 0 & 0 \\ 0 & 0 & \frac{\cos\sigma^L}{U} & -\frac{\sin\sigma^L}{U} \\ 0 & 0 & \frac{\sin\sigma^L}{U} & \frac{\cos\sigma^L}{U} \end{pmatrix}, \tag{A4}$$

with

$$\begin{aligned} m_z &= \frac{i}{2}\frac{\alpha_y}{\alpha_z}\left(1+\alpha_z^2\right), \\ n_z &= \frac{i}{2}\frac{\alpha_y}{\alpha_z}, \\ U &= \exp[-i(2\pi/\lambda)N\alpha_z d], \\ \sigma^P &= (\pi/\lambda)NQd, \\ \sigma^L &= (\pi/\lambda)NQd\alpha_y/\alpha_z, \end{aligned} \tag{A5}$$

where α_y and α_z are the cosine and sine of the incident angle for the medium, N is the complex refractive index, d is the film thickness, Q is the MO coupling constant, and λ is the light wavelength.

APPENDIX B: APPROXIMATE SOLUTIONS OF KERR SIGNALS WITH THE FO POSTSELECTION

In this paper, we employ MATHEMATICA as a powerful computational tool to analytically solve the equation

$$A_{w0} = \frac{\langle \Psi_{f0}|\hat{A}|\Psi_w\rangle}{\langle \Psi_{f0}|\Psi_w\rangle} = \frac{e^{+\theta_k+i\varepsilon}+e^{-\theta_k-i\varepsilon}}{e^{+\theta_k+i\varepsilon}-e^{-\theta_k-i\varepsilon}} = \mathrm{Re}A_{w0}+i\mathrm{Im}A_{w0}. \tag{B1}$$

To simplify the expression of the formula, we introduce a simplification by defining

$$a_0 = \mathrm{Re}A_{w0}^2+2\mathrm{Re}A_{w0}+\mathrm{Im}A_{w0}^2+1,$$
$$b_0 = \mathrm{Re}A_{w0}^2-2\mathrm{Re}A_{w0}+\mathrm{Im}A_{w0}^2+1. \tag{B2}$$

The derivation of the approximate solution for Kerr rotation θ_k with the FO postselection is obtained from Eq. (B1) in the following:

$$\theta_k = \frac{1}{4}\log\left(\frac{a_0}{b_0}\right) = \frac{1}{4}\log\left(\frac{b_0+4\mathrm{Re}A_{w0}}{b_0}\right),$$
$$e^{4\theta_k} = 1+\frac{4\mathrm{Re}A_{w0}}{\mathrm{Re}A_{w0}^2-2\mathrm{Re}A_{w0}+\mathrm{Im}A_{w0}^2+1}. \tag{B3}$$

By employing the approximation $e^{4\theta_k}\approx 1+4\theta_k$ when $\theta_k \ll 1$, we obtain

$$1+4\theta_k \approx 1+\frac{4\mathrm{Re}A_{w0}}{\mathrm{Re}A_{w0}^2-2\mathrm{Re}A_{w0}+\mathrm{Im}A_{w0}^2+1} = 1+\frac{4}{\mathrm{Re}A_{w0}-2+\frac{\mathrm{Im}A_{w0}^2}{\mathrm{Re}A_{w0}}+\frac{1}{\mathrm{Re}A_{w0}}},$$
$$\theta_k = \frac{1}{\mathrm{Re}A_{w0}-2+\frac{\mathrm{Im}A_{w0}^2}{\mathrm{Re}A_{w0}}+\frac{1}{\mathrm{Re}A_{w0}}}. \tag{B4}$$

Then, we can derive an approximate solution for Kerr rotation θ_k, along with the expression given in Eq. (11) in the main text

$$\theta_k \approx \frac{1}{\mathrm{Re}A_{w0}}. \tag{B5}$$

This approximation is valid under the approximate conditions of $\mathrm{Re}A_{w0}\gg 1$ and $\mathrm{Re}A_{w0}/\mathrm{Im}A_{w0}\gg 1$.

Meanwhile, Kerr ellipticity ε with the FO postselection can be derived as follows:

$$\varepsilon = \frac{1}{2}\mathrm{ArcTan}\left(\frac{\mathrm{Re}A_{w0}^2+\mathrm{Im}A_{w0}^2-1}{\sqrt{b_0}\sqrt{a_0}}, -\frac{2\mathrm{Im}A_{w0}}{\sqrt{b_0}\sqrt{a_0}}\right) = \frac{1}{2}\mathrm{ArcTan}\left(\frac{-2\mathrm{Im}A_{w0}}{-1+\mathrm{Re}A_{w0}^2+\mathrm{Im}A_{w0}^2}\right)$$
$$= -\frac{1}{2}\mathrm{ArcTan}\left(\frac{2}{-\frac{1}{\mathrm{Im}A_{w0}}+\frac{\mathrm{Re}A_{w0}^2}{\mathrm{Im}A_{w0}}+\mathrm{Im}A_{w0}}\right). \tag{B6}$$

By taking into account the approximate conditions of $\mathrm{Im}A_{w0}\gg 1$ and $\mathrm{Re}A_{w0}/\mathrm{Im}A_{w0}\ll 1$, we can derive Eq. (12) in the main text through the following calculation:

$$\varepsilon \approx -\frac{1}{2}\mathrm{ArcTan}\left(\frac{2}{\mathrm{Im}A_{w0}}\right) \approx -\frac{1}{\mathrm{Im}A_{w0}}. \tag{B7}$$

APPENDIX C: APPROXIMATE SOLUTIONS OF KERR SIGNALS WITH THE NON-FO POSTSELECTION

In our investigation of the non-FO postselection scenario, we also utilize MATHEMATICA to analytically solve Eq. (14) presented in the main text. To improve the clarity of the formula, we introduce a simplification by defining

$$a_1 = \mathrm{Re}A_{w1}{}^2+\mathrm{Im}A_{w1}{}^2+1,$$
$$b_1 = \mathrm{Re}A_{w1}{}^2-2\mathrm{Re}A_{w1}+\mathrm{Im}A_{w1}{}^2+1,$$
$$a_2 = \mathrm{Re}A_{w2}{}^2+\mathrm{Re}A_{w2}+\mathrm{Im}A_{w2}{}^2,$$
$$b_2 = \mathrm{Re}A_{w2}{}^2-2\mathrm{Re}A_{w2}+\mathrm{Im}A_{w2}{}^2+1,$$
$$c_2 = \mathrm{Re}A_{w2}\cos^2(2\gamma_2),$$
$$d_2 = \mathrm{Re}A_{w2}{}^2+\mathrm{Im}A_{w2}{}^2+1,$$
$$e_2 = \mathrm{Re}A_{w2}\cos(4\gamma_2)+\mathrm{Re}A_{w2}. \tag{C1}$$

The derivation of the approximate solution of Kerr rotation θ_k, considering the non-FO postselected parameters γ_1 and η_1, is presented as follows:

$$\theta_k = \frac{1}{4}\log\left(\frac{4\mathrm{Re}A_{w1}\cos^2(2\gamma_1)+[\cos(4\gamma_1)+1]a_1}{2[\sin(2\gamma_1)-1]^2(b_1)}\right). \tag{C2}$$

By approximating $\cos(4\gamma_1)$ as 1, the expression in Eq. (C2) can be further simplified, leading to the following form:

$$\theta_k \approx \frac{1}{4}\log\left(\frac{4\mathrm{Re}A_{w1}\cos^2(2\gamma_1)+4\mathrm{Re}A_{w1}+(2b_1)}{2[\sin(2\gamma_1)-1]2b_1}\right)$$
$$= \frac{1}{4}\log\left(\frac{4\mathrm{Re}A_{w1}+4\mathrm{Re}A_{w1}\cos^2(2\gamma_1)}{2[\sin(2\gamma_1)-1]^2b_1}+\frac{1}{[1-\sin(2\gamma_1)]^2}\right)$$
$$= \frac{1}{4}\log\left(\frac{2\mathrm{Re}A_{w1}[1+\cos^2(2\gamma_1)]}{[\sin(2\gamma_1)-1]^2b_1}+\frac{1}{[1-\sin(2\gamma_1)]^2}\right). \tag{C3}$$

Subsequently, by taking into account the approximate condition of $\sin(2\gamma_1)=0$, Eq. (C3) can be simplified to the following expression:

$$\theta_k \approx \frac{1}{4}\log\left(\frac{2\mathrm{Re}A_{w1}[1+\cos^2(2\gamma_1)]}{b_1}+1\right),$$
$$e^{4\theta_k} = \frac{2\mathrm{Re}A_{w1}[1+\cos^2(2\gamma_1)]}{b_1}+1. \tag{C4}$$

By employing the approximation $e^{4\theta_k}\approx 1+4\theta_k$ when $\theta_k \ll 1$, we then obtain

$$1+4\theta_k \approx \frac{2\mathrm{Re}A_{w1}[1+\cos^2(2\gamma_1)]}{b_1}+1,$$
$$\theta_k = \frac{1}{4}\frac{[1+\cos^2(2\gamma_1)]}{\mathrm{Re}A_{w1}-2+\frac{\mathrm{Im}A_{w1}{}^2}{\mathrm{Re}A_{w1}}+\frac{1}{\mathrm{Re}A_{w1}}}. \tag{C5}$$

Finally, with the approximate conditions of $\mathrm{Re}A_{w1} \gg 1$ and $\mathrm{Re}A_{w1}/\mathrm{Im}A_{w1} \gg 1$, we can derive Eq. (15) as follows:

$$\theta_k \approx \frac{1+\cos^2(2\gamma_1)}{2\mathrm{Re}A_{w1}}. \tag{C6}$$

Similarly, we can derive the approximate solution for Kerr ellipticity, as presented in Eq. (16) in the main text, in the following:

$$\varepsilon = \eta_2 + \frac{1}{2}\mathrm{Arctan}\left[\left(\frac{\mathrm{Re}A_{w2}{}^3 - 2\mathrm{Re}A_{w2}c_2 - 2c_2}{-\mathrm{Im}A_{w2}(2c_2+e_2)} + \frac{\mathrm{Re}A_{w2}\cos(4\gamma_2)(a_2) + \mathrm{Re}A_{w2}{}^2 + \mathrm{Re}A_{w2}\mathrm{Im}A_{w2}{}^2}{-\mathrm{Im}A_{w2}(2c_2+e_2)}\right)^{-1}\right]. \tag{C7}$$

The expression in Eq. (C7) can be simplified by approximating $\cos(4\gamma_1)$ as 1, resulting in

$$\varepsilon \approx \eta_2 - \frac{1}{2}\left(\frac{2\frac{\mathrm{Re}A_{w2}{}^2}{\mathrm{Im}A_{w2}} - \frac{2\mathrm{Re}A_{w2}{}^2}{\mathrm{Im}A_{w2}}[1+\cos^2(2\gamma_2)]}{1+\cos^2(2\gamma_2)} + \frac{-\frac{2\cos^2(2\gamma_2)}{\mathrm{Im}A_{w2}} + \mathrm{Im}A_{w2} + \mathrm{Re}A_{w2}}{1+\cos^2(2\gamma_2)}\right)^{-1}. \tag{C8}$$

Finally, Eq. (16) in the main text can be obtained with the approximate conditions of $\mathrm{Im}A_{w2} \gg 1$ and $\mathrm{Im}A_{w2}/\mathrm{Re}A_{w2} \gg 1$:

$$\varepsilon \approx \eta_2 - \frac{1+\cos^2(2\gamma_2)}{2\mathrm{Im}A_{w2}}. \tag{C9}$$

[1] Z. Q. Qiu and S. D. Bader, Surface magneto-optic Kerr effect, Rev. Sci. Instrum. **71**, 1243 (2000).

[2] J. Kerr, XXIV. On reflection of polarized light from the equatorial surface of a magnet, Lond. Edinb. Dublin Philos. Mag. J. Sci. **5**, 161 (1878).

[3] S. D. Bader, E. R. Moog, and P. Grünberg, Magnetic hysteresis of epitaxially-deposited iron in the monolayer range: A Kerr effect experiment in surface magnetism, J. Magn. Magn. Mater. **53**, L295 (1986).

[4] G. Vinai, F. Motti, A. Yu. Petrov, V. Polewczyk, V. Bonanni, R. Edla, B. Gobaut, J. Fujii, F. Suran, D. Benedetti, F. Salvador, A. Fondacaro, G. Rossi, G. Panaccione, B. A. Davidson, and P. Torelli, An integrated ultra-high vacuum apparatus for growth and in situ characterization of complex materials, Rev. Sci. Instrum. **91**, 085109 (2020).

[5] X. D. Zhu, R. Ullah, and V. Taufour, Oblique-incidence sagnac interferometric scanning microscope for studying magneto-optic effects of materials at low temperatures, Rev. Sci. Instrum. **92**, 043706 (2021).

[6] T. Taniuchi, Y. Motoyui, K. Morozumi, T. C. Rödel, F. Fortuna, A. F. Santander-Syro, and S. Shin, Imaging of room-temperature ferromagnetic nano-domains at the surface of a non-magnetic oxide, Nat. Commun. **7**, 11781 (2016).

[7] K. Fleischer, N. Thiyagarajah, Y.-C. Lau, D. Betto, K. Borisov, C. C. Smith, I. V. Shvets, J. M. D. Coey, and K. Rode, Magneto-optic Kerr effect in a spin-polarized zero-moment ferrimagnet, Phys. Rev. B **98**, 134445 (2018).

[8] A. Sharma, M. A. Hoffmann, P. Matthes, O. Hellwig, C. Kowol, S. E. Schulz, D. R. T. Zahn, and G. Salvan, Crystallization of optically thick films of $Co_xFe_{80-x}B_{20}$: Evolution of optical, magneto-optical, and structural properties, Phys. Rev. B **101**, 054438 (2020).

[9] M. H. Burkhardt, M. A. Hossain, S. Sarkar, Y.-D. Chuang, A. G. Cruz Gonzalez, A. Doran, A. Scholl, A. T. Young, N. Tahir, Y. J. Choi, S.-W. Cheong, H. A. Dürr, and J. Stöhr, Imaging the First-Order Magnetic Transition in $La_{0.35}Pr_{0.275}Ca_{0.375}MnO_3$, Phys. Rev. Lett. **108**, 237202 (2012).

[10] A. Fernández-Pacheco, R. Streubel, O. Fruchart, R. Hertel, P. Fischer, and R. P. Cowburn, Three-dimensional nanomagnetism, Nat. Commun. **8**, 15756 (2017).

[11] A. Mitrofanov, G. Chen, A. Kozhanov, and S. Urazhdin, Exchange bias without directional anisotropy in permalloy/CoO bilayers, Phys. Rev. B **104**, 144413 (2021).

[12] S. A. R. Horsley, Indifferent electromagnetic modes: Bound states and topology, Phys. Rev. A **100**, 053819 (2019).

[13] T. Van Mechelen, W. Sun, and Z. Jacob, Optical N-invariant of graphene's topological viscous Hall fluid, Nat. Commun. **12**, 4729 (2021).

[14] S. Melle, J. L. Menéndez, G. Armelles, D. Navas, M. Vázquez, K. Nielsch, R. B. Wehrspohn, and U. Gösele, Magneto-optical properties of nickel nanowire arrays, Appl. Phys. Lett. **83**, 4547 (2003).

[15] G. S. Jenkins, A. B. Sushkov, D. C. Schmadel, N. P. Butch, P. Syers, J. Paglione, and H. D. Drew, Terahertz Kerr and reflectivity measurements on the topological insulator Bi_2Se_3, Phys. Rev. B **82**, 125120 (2010).

[16] N. Qureshi, S. Wang, M. A. Lowther, A. R. Hawkins, S. Kwon, A. Liddle, J. Bokor, and H. Schmidt, Cavity-enhanced magnetooptical observation of magnetization reversal in individual single-domain nanomagnets, Nano Lett. **5**, 1413 (2005).

[17] S. Y. Zhang, J. L. Gao, W. B. Xia, X. J. Luo, S. L. Tang, and Y. W. Du, Giant magneto-optical Kerr effect in HfO_2/Co/HfO_2/Al/silicon structure, J. Appl. Phys. **114**, 064308 (2013).

[18] X. Wang and C. Y. Cui, Cavity enhancement simulation of the magneto-optical Kerr effect in optically anisotropic multilayer structure, Optik **181**, 123 (2019).

[19] M. Moradi and M. Ghanaatshoar, Cavity enhancement of the magneto-optic Kerr effect in glass/Al/SnO_2/PtMnSb/SnO_2 structure, Opt. Commun. **283**, 5053 (2010).

[20] V. I. Belotelov, I. A. Akimov, M. Pohl, V. A. Kotov, S. Kasture, A. S. Vengurlekar, A. V. Gopal, D. R. Yakovlev, A. K. Zvezdin, and M. Bayer, Enhanced magneto-optical effects in magnetoplasmonic crystals, Nat. Nanotechnol. **6**, 370 (2011).

[21] G. Armelles, A. Cebollada, A. García-Martín, and M. U. González, Magnetoplasmonics: Combining magnetic and plasmonic functionalities, Adv. Opt. Mater. **1**, 10 (2013).

[22] J. Qin, S. Xia, W. Yang, H. Wang, W. Yan, Y. Yang, Z. Wei, W. Liu, Y. Luo, L. Deng, and L. Bi, Nanophotonic devices

based on magneto-optical materials: recent developments and applications, Nanophotonics **11**, 2639 (2022).
[23] J. Dressel, M. Malik, F. M. Miatto, A. N. Jordan, and R. W. Boyd, Colloquium: Understanding quantum weak values: Basics and applications, Rev. Mod. Phys. **86**, 307 (2014).
[24] S. Kocsis, B. Braverman, S. Ravets, M. J. Stevens, R. P. Mirin, L. K. Shalm, and A. M. Steinberg, Observing the average trajectories of single photons in a two-slit interferometer, Science **332**, 1170 (2011).
[25] J. S. Lundeen, B. Sutherland, A. Patel, C. Stewart, and C. Bamber, Direct measurement of the quantum wavefunction, Nature (London) **474**, 188 (2011).
[26] L. Li, Y. Li, Y.-L. Zhang, S. Yu, C.-Y. Lu, N.-L. Liu, J. Zhang, and J.-W. Pan, Phase amplification in optical interferometry with weak measurement, Phys. Rev. A **97**, 033851 (2018).
[27] J.-H. Huang, X.-Y. Hu, A. C. Dada, J. S. Lundeen, K. M. Jordan, H. Chen, and J. An, Autocorrelative weak-value amplification and simulating the protocol under strong gaussian noise, Phys. Rev. A **106**, 053704 (2022).
[28] S. Harraz, S. Cong, and J. J. Nieto, Enhancing quantum teleportation fidelity under decoherence via weak measurement with flips, EPJ Quantum Technol. **9**, 15 (2022).
[29] J.-H. Huang, F.-F. He, X.-Y. Duan, G.-J. Wang, and X.-Y. Hu, A potential third-generation gravitational-wave detector based on autocorrelative weak-value amplification, Class. Quantum Grav. **40**, 185003 (2023).
[30] B. Xia, J. Huang, H. Li, H. Wang, and G. Zeng, Toward incompatible quantum limits on multiparameter estimation, Nat. Commun. **14**, 1021 (2023).
[31] Y. Aharonov, D. Z. Albert, and L. Vaidman, How the Result of a Measurement of a Component of the Spin of a Spin- *1/2* Particle Can Turn Out to be 100, Phys. Rev. Lett. **60**, 1351 (1988).
[32] O. S. Magana-Loaiza, M. Mirhosseini, B. Rodenburg, and R. W. Boyd, Amplification of Angular Rotations Using Weak Measurements, Phys. Rev. Lett. **112**, 200401 (2014).
[33] P. B. Dixon, D. J. Starling, A. N. Jordan, and J. C. Howell, Ultrasensitive Beam Deflection Measurement via Interferometric Weak Value Amplification, Phys. Rev. Lett. **102**, 173601 (2009).
[34] D. J. Starling, P. B. Dixon, A. N. Jordan, and J. C. Howell, Optimizing the signal-to-noise ratio of a beam-deflection measurement with interferometric weak values, Phys. Rev. A **80**, 041803(R) (2009).
[35] J.-H. Huang, F.-F. He, X.-Y. Duan, G.-J. Wang, and X.-Y. Hu, Modified weak-value-amplification technique for measuring a mirror's velocity based on the Vernier effect, Phys. Rev. A **105**, 013718 (2022).
[36] Y. Liu, Y. Zhang, Z. Xu, L. Zhou, Y. Zou, B. Zhang, and Z. Hu, Ultra-low noise phase measurement of fiber optic sensors via weak value amplification, Opt. Express **30**, 18966 (2022).
[37] D. Li, C. Weng, C. Chen, K. Li, Q. Lin, Y. Ruan, J. Zhang, S. Wang, and J. Yao, Optical biosensor based on weak value amplification for the high sensitivity detection of Pertuzumab in combination with Trastuzumab binding to the extracellular domain of HER2, Opt. Express **30**, 36839 (2022).
[38] H. Luo, X. Zhou, W. Shu, S. Wen, and D. Fan, Enhanced and switchable spin Hall effect of light near the Brewster angle on reflection, Phys. Rev. A **84**, 043806 (2011).
[39] J. Li, T. Tang, L. Luo, J. Shen, C. Li, J. Qin, and L. Bi, Weak measurement of the magneto-optical spin Hall effect of light, Photon. Res. **7**, 1014 (2019).
[40] Q. Wang, T. Li, L. Luo, Y. He, X. Liu, Z. Li, Z. Zhang, and J. Du, Measurement of hysteresis loop based on weak measurement, Opt. Lett. **45**, 1075 (2020).
[41] Y. He, L. Luo, L. Xie, J. Shao, Y. Liu, J. You, Y. Ye, and Z. Zhang, Detection of magneto-optical Kerr signals via weak measurement with frequency pointer, Opt. Lett. **46**, 4140 (2021).
[42] L. Luo, T. Li, Y. Jiang, L. Fang, B. Liu, and Z. Zhang, Estimation of kerr angle based on weak measurement with two pointers, Opt. Express **31**, 14432 (2023).
[43] J. Zak, E. R. Moog, C. Liu, and S. D. Bader, Universal approach to magneto-optics, J. Magn. Magn. Mater. **89**, 107 (1990).
[44] D. Li, T. Guan, F. Liu, A. Yang, Y. He, Q. He, Z. Shen, and M. Xin, Optical rotation based chirality detection of enantiomers via weak measurement in frequency domain, Appl. Phys. Lett. **112**, 213701 (2018).
[45] K. Balasubramanian, A. S. Marathay, and H. A. Macleod, Modeling magneto-optical thin film media for optical data storage, Thin Solid Films **164**, 391 (1988).
[46] Y. Souche, V. Novosad, B. Pannetier, and O. Geoffroy, Magneto-optical diffraction and transverse Kerr effect, J. Magn. Magn. Mater. **177-181**, 1277 (1998).
[47] V. I. Belotelov, D. A. Bykov, L. L. Doskolovich, A. N. Kalish, and A. K. Zvezdin, Extraordinary transmission and giant magneto-optical transverse Kerr effect in plasmonic nanostructured films, J. Opt. Soc. Am. B **26**, 1594 (2009).
[48] S. Flewett, E. Burgos-Parra, M. Garrido Strelow, Y. Sassi, C. Léveillé, F. Ajejas, N. Reyren, and N. Jaouen, General treatment of off-specular resonant soft x-ray magnetic scattering using the distorted-wave born approximation: Numerical algorithm and experimental studies with hybrid chiral domain structures, Phys. Rev. B **103**, 184401 (2021).
[49] E. Cordero and K. Gröchenig, Time-frequency analysis of localization operators, J. Funct. Anal. **205**, 107 (2003).
[50] S. R. Greenfield and M. R. Wasielewski, Near-transform-limited visible and near-IR femtosecond pulses from optical parametric amplification using Type II β-barium borate, Opt. Lett. **20**, 1394 (1995).
[51] V. Scardaci, Z. Sun, F. Wang, A. G. Rozhin, T. Hasan, F. Hennrich, I. H. White, W. I. Milne, and A. C. Ferrari, Carbon nanotube polycarbonate composites for ultrafast lasers, Adv. Mater. **20**, 4040 (2008).
[52] Q. Yan, Q. Deng, J. Zhang, Y. Zhu, K. Yin, T. Li, D. Wu, and T. Jiang, Low-latency deep-reinforcement learning algorithm for ultrafast fiber lasers, Photon. Res. **9**, 1493 (2021).
[53] X.-Y. Xu, Y. Kedem, K. Sun, L. Vaidman, C.-F. Li, and G.-C. Guo, Phase Estimation with Weak Measurement Using a White Light Source, Phys. Rev. Lett. **111**, 033604 (2013).
[54] C. Fang, J.-Z. Huang, Y. Yu, Q. Li, and G. Zeng, Ultra-small time-delay estimation via a weak measurement technique with post-selection, J. Phys. B: At. Mol. Opt. Phys. **49**, 175501 (2016).
[55] J. Zhu, Z. Li, Y. Liu, Y. Ye, Q. Ti, Z. Zhang, and F. Gao, Weak measurement with the peak-contrast-ratio pointer, Phys. Rev. A **103**, 032212 (2021).

[56] Y. Susa, Y. Shikano, and A. Hosoya, Optimal probe wave function of weak-value amplification, Phys. Rev. A **85**, 052110 (2012).

[57] K. Nakamura, A. Nishizawa, and M.-K. Fujimoto, Evaluation of weak measurements to all orders, Phys. Rev. A **85**, 012113 (2012).

[58] The database about complex refractive indices for various materials as a function of electromagnetic wavelength, see http://refractiveindex.info/.

[59] R. M. Osgood, K. T. Riggs, A. E. Johnson, J. E. Mattson, C. H. Sowers, and S. D. Bader, Magneto-optic constants of hcp and fcc Co films, Phys. Rev. B **56**, 2627 (1997).

[60] Thorlabs' FiberBench Precision Rotating Linear Polarizer can offer vernier scale with 10 arcmin resolution, see https://www.thorlabs.de/newgrouppage9.cfm?objectgroup_id=3101.

[61] Thorlabs' the Soleil-Babinet Compensator is a continuously variable, zero-order retarder (wave plate) that operates over a broad wavelength range, see https://www.thorlabs.de/newgrouppage9.cfm?objectgroup_id=871.

[62] M. Raghuramaiah, A. K. Sharma, P. A. Naik, P. D. Gupta, and R. A. Ganeev, A second-order autocorrelator for single-shot measurement of femtosecond laser pulse durations, Sadhana **26**, 603 (2001).

[63] J. Mu, X. Wang, F. Jing, Q. H. Zhu, J. Q. Su, and J. W. Zhang, Analysis of the synchronization error measurement via non-collinear cross-correlation, Laser Part. Beams **33**, 355 (2015).

[64] J. Harris, R. W. Boyd, and J. S. Lundeen, Weak Value Amplification Can Outperform Conventional Measurement in the Presence of Detector Saturation, Phys. Rev. Lett. **118**, 070802 (2017).

[65] S. Wang, A. Barman, H. Schmidt, J. D. Maas, A. R. Hawkins, S. Kwon, B. Harteneck, S. Cabrini, and J. Bokor, Optimization of nano-magneto-optic sensitivity using dual dielectric layer enhancement, Appl. Phys. Lett. **90**, 252504 (2007).

[66] V. G. Kravets and A. S. Lapchuk, Enhancement of magneto-optical effects in magnetic nanoparticles near gold-dielectric surfaces, Appl. Opt. **49**, 5013 (2010).

[67] A. Berger and M. R. Pufall, Generalized magneto-optical ellipsometry, Appl. Phys. Lett. **71**, 965 (1997).

[68] Y. Turek, H. Kobayashi, T. Akutsu, C.-P. Sun, and Y. Shikano, Post-selected von Neumann measurement with Hermite-Gaussian and Laguerre-Gaussian pointer states, New J. Phys. **17**, 083029 (2015).

[69] B. Xia, J. Huang, C. Fang, H. Li, and G. Zeng, High-Precision Multiparameter Weak Measurement with Hermite-Gaussian Pointer, Phys. Rev. Appl. **13**, 034023 (2020).

[70] S. Pang, J. R. G. Alonso, T. A. Brun, and A. N. Jordan, Protecting weak measurements against systematic errors, Phys. Rev. A **94**, 012329 (2016).

[71] M. Zhang, J. Zhang, C. Wu, Y. Xie, T. Chen, W. Wu, and P. Chen, Optimization of parameter measurement precision with precoupling-assisted weak-value amplification, Phys. Rev. A **107**, 042601 (2023).

[72] Y. Liu, L. Qin, and X.-Q. Li, Fisher information analysis on weak-value-amplification metrology using optical coherent states, Phys. Rev. A **106**, 022619 (2022).

[73] J. Zak, E. R. Moog, C. Liu, and S. D. Bader, Magneto-optics of multilayers with arbitrary magnetization directions, Phys. Rev. B **43**, 6423 (1991).